Investigating the young AU Mic system with SPIRou: large-scale stellar magnetic field and close-in planet mass

Baptiste Klein, Jean-François Donati, Claire Moutou, Xavier Delfosse, Xavier Bonfils, Eder Martioli, Pascal Fouqué, Ryan Cloutier, Étienne Artigau, René Doyon, et al.

▶ **To cite this version:**

Baptiste Klein, Jean-François Donati, Claire Moutou, Xavier Delfosse, Xavier Bonfils, et al.. Investigating the young AU Mic system with SPIRou: large-scale stellar magnetic field and close-in planet mass. Monthly Notices of the Royal Astronomical Society: Letters, 2020, 502 (1), pp.188-205. 10.1093/mnras/staa3702 . hal-03034443

HAL Id: hal-03034443
https://cnrs.hal.science/hal-03034443

Submitted on 2 Feb 2021

HAL is a multi-disciplinary open access archive for the deposit and dissemination of scientific research documents, whether they are published or not. The documents may come from teaching and research institutions in France or abroad, or from public or private research centers.

L'archive ouverte pluridisciplinaire **HAL**, est destinée au dépôt et à la diffusion de documents scientifiques de niveau recherche, publiés ou non, émanant des établissements d'enseignement et de recherche français ou étrangers, des laboratoires publics ou privés.

Monthly Notices of the ROYAL ASTRONOMICAL SOCIETY

MNRAS **502,** 188–205 (2021) doi:10.1093/mnras/staa3702
Advance Access publication 2020 December 8

Investigating the young AU Mic system with SPIRou: large-scale stellar magnetic field and close-in planet mass

Baptiste Klein [1★] Jean-François Donati [1] Claire Moutou,[1] Xavier Delfosse,[2] Xavier Bonfils,[2] Eder Martioli,[3,4] Pascal Fouqué [1,5] Ryan Cloutier [6] Étienne Artigau,[7] René Doyon,[7] Guillaume Hébrard,[3] Julien Morin,[8] Julien Rameau,[2] Peter Plavchan [9] and Eric Gaidos [10★]

[1] *Université de Toulouse, CNRS, IRAP, 14 av. Belin, F-31400 Toulouse, France*
[2] *CNRS, IPAG, Université Grenoble Alpes, F-38000 Grenoble, France*
[3] *Institut dAstrophysique de Paris, UMR7095 CNRS, Université Pierre and Marie Curie, 98bis boulevard Arago, F-75014 Paris, France*
[4] *Laboratorio Nacional de Astrofisica (LNA/MCTI), Rua Estados Unidos, 154, Itajuba, MG, Brazil*
[5] *CFHT Corporation, 65-1238 Mamalahoa Hwy, Kamuela, HI 96743, USA*
[6] *Center for Astrophysics | Harvard and Smithsonian, 60 Garden Street, Cambridge, MA 02138, USA*
[7] *Institut de Recherche sur les Exoplanètes (IREx), Département de Physique, Université de Montréal, C.P. 6128, Succ. Centre-Ville, Montréal, QC H3C 3J7, Canada*
[8] *LUPM, Université de Montpellier, CNRS, Place Eugène Bataillon, F-34095 Montpellier, France*
[9] *Department of Physics and Astronomy, George Mason University, Fairfax, VA 22030, USA*
[10] *Department of Earth Sciences, University of Hawai'i at Manoa, Honoluu, HI 96822, USA*

Accepted 2020 November 22. Received 2020 November 13; in original form 2020 June 22

ABSTRACT

We present a velocimetric and spectropolarimetric analysis of 27 observations of the 22-Myr M1 star AU Microscopii (AU Mic) collected with the high-resolution *YJHK* (0.98–2.35 μm) spectropolarimeter SPIRou from 2019 September 18 to November 14. Our radial velocity (RV) time-series exhibits activity-induced fluctuations of 45 m s^{-1} rms, ∼3 times smaller than those measured in the optical domain, that we filter using Gaussian Process Regression. We report a 3.9σ detection of the recently discovered 8.46 -d transiting planet AU Mic b, with an estimated mass of $17.1^{+4.7}_{-4.5}$ M$_\oplus$ and a bulk density of 1.3 ± 0.4 g cm^{-3}, inducing an RV signature of semi-amplitude $K = 8.5^{+2.3}_{-2.2}$ m s^{-1} in the spectrum of its host star. A consistent detection is independently obtained when we simultaneously image stellar surface inhomogeneities and estimate the planet parameters with Zeeman–Doppler imaging (ZDI). Using ZDI, we invert the time-series of unpolarized and circularly polarized spectra into surface brightness and large-scale magnetic maps. We find a mainly poloidal and axisymmetric field of 475 G, featuring, in particular, a dipole of 450 G tilted at 19° to the rotation axis. Moreover, we detect a strong differential rotation of $d\Omega = 0.167 \pm 0.009$ rad d^{-1} shearing the large-scale field, about twice stronger than that shearing the brightness distribution, suggesting that both observables probe different layers of the convective zone. Even though we caution that more RV measurements are needed to accurately pin down the planet mass, AU Mic b already appears as a prime target for constraining planet formation models, studying the interactions with the surrounding debris disc, and characterizing its atmosphere with upcoming space- and ground-based missions.

Key words: techniques: polarimetric – techniques: radial velocities – planets and satellites: formation – stars: imaging – stars: individual: AU Microscopii – stars: magnetic fields.

1 INTRODUCTION

Close-in planetary systems orbiting and transiting pre-main-sequence (PMS) stars are key targets to improve our understanding of how planets form and evolve. Their orbital parameters (e.g. orbit ellipticity and spin–orbit obliquity) and the composition of their atmosphere can yield essential information about their formation history (Baruteau et al. 2016; Madhusudhan 2019). Moreover, the evolution of their bulk density during the early stages of their lives is critically needed to constrain planet formation and evolution models (e.g. Alibert et al. 2005; Mordasini et al. 2012a, b). This requires to precisely measure both planet masses, by monitoring the radial velocity (RV) of their host star, and radii, through the relative depth of their photometric transit curve.

PMS stars, however, exhibit intense magnetic activity whose underlying dynamo processes are not fully understood yet (e.g. Donati et al. 2014; Yu et al. 2019; Hill et al. 2019). This activity generates large bright and dark features at the surface of the star, leading to fluctuations in both photometric and RV curves that are much stronger than planet signatures, rendering them extremely difficult to detect. As a consequence, only a few close-in newborn planets have been unveiled so far, none of them having a well-constrained bulk density (see Donati et al. 2016;

★ E-mail: baptiste.klein@irap.omp.eu (BK); gaidos@hawaii.edu (EG)

© 2020 The Author(s)
Published by Oxford University Press on behalf of Royal Astronomical Society

Downloaded from https://academic.oup.com/mnras/article/502/1/188/6027693 by CNRS - ISTO user on 02 February 2021

Johns-Krull et al. 2016; David et al. 2016; Mann et al. 2016; Yu et al. 2017; David et al. 2019a, b, only two of these systems are transiting).

AU Microscopii (AU Mic, GJ 803, HD 197481, HIP 102409) is an active nearby ($d = 9.72$ pc) M1 PMS star located in the ∼22 Myr-old β Pic moving group (Mamajek & Bell 2014; Malo et al. 2014; Messina et al. 2016). The star has been widely studied over the past decades for its intense magnetic activity generating numerous phenomena, for example, ∼0.1 mag photometric variations in the visible domain (e.g. Torres & Ferraz Mello 1973; Rodono et al. 1986). AU Mic hosts a resolved edge-on debris disc at distances ranging from ∼35 to 210 au, offering an excellent framework to study planet formation and evolution (e.g. Kalas, Liu & Matthews 2004; Wilner et al. 2012; MacGregor et al. 2013; Matthews et al. 2015; Daley et al. 2019). Asymmetric fast moving structures have been discovered in AU Mic's debris disc (Boccaletti et al. 2015, 2018; Daley et al. 2019). The origin of these features, tentatively explained by interactions between the stellar wind and the disc (Chiang & Fung 2017), or the presence of a massive body in the inner region of the disc (Sezestre et al. 2017), remains unclear. A close-in transiting Neptune-sized planet was newly detected around AU Mic from photometric observations collected with *TESS* and *Spitzer* space missions (Plavchan et al. 2020, hereafter P20). Given the brightness of the star and the relatively small semimajor axis of the planet orbit (0.066 au), AU Mic b stands as the best transiting PMS target for a velocimetric mass measurement. However, RV time-series measured from spectra covering the optical wavelength domain exhibit large activity-induced fluctuations of 115–175 m s^{-1} rms, leading P20 to report no more than an upper limit of 3.4 $M_{\Neptune}$ (58.3 $M_\oplus$) for the mass of AU Mic b (where $M_{\Neptune}$ denotes the mass of Neptune).

The near-infrared (nIR) spectropolarimeter SPIRou at the Canada–France–Hawaii telescope (CFHT, Donati et al. 2018, 2020) is the ideal instrument to detect AU Mic b and measure its mass. Its high resolving power of ∼70 000 throughout the *YJHK* spectral bands (i.e. 0.98–2.35 nm) makes it well suited to provide precise RVs for as bright a star as AU Mic ($H = 4.831$; Cutri et al. 2003). Moreover, the RV signal generated by stellar activity for PMS stars is expected to be significantly weaker in the nIR than in the optical domain (Mahmud et al. 2011; Crockett et al. 2012; Klein & Donati 2020), making it easier to separate from the planet signature. Thanks to its spectropolarimetric capabilities, SPIRou has the additional potential to detect and reconstruct the surface topology of the large-scale magnetic field of AU Mic (Donati & Landstreet 2009), allowing one not only to filter RV curves from the modelled activity, but also to constrain the underlying dynamo processes.

In this study, we present velocimetric and spectropolarimetric data of AU Mic consisting of 27 unpolarized and circularly polarized spectra collected with SPIRou from 2019 September 18 to November 14. The observations and the data reduction are described in Section 2. In Section 3, we detail the RV measurement process as well as the detection of a planet signature from our RV time-series. In Section 4, we present independent methods based on Zeeman–Doppler imaging (ZDI) to confirm the planet signature while filtering the stellar activity. The inversion of unpolarized and circularly polarized profiles into brightness and large-scale magnetic maps is detailed in Section 5. Finally, we investigate the chromospheric activity of the star and its correlation with the magnetic map and RV time-series in Section 6, before discussing, in Section 7, the impact of these results on our understanding of star/planet formation.

Table 1. Journal of spectropolarimetric observations of AU Mic with SPIRou. All polarization sequences consist of four individual exposures of 195 s each. The first column lists the BJDs at mid-exposure (the first and last observations corresponding respectively to September 18 and November 14). In columns 2–4, we respectively give the peak S/N (per pixel, i.e. 2.28 km s^{-1} velocity bin) and the rms noise level in Stokes I and V LSD profiles (respectively, called $\sigma_{\rm I}$ and $\sigma_{\rm V}$; note that $\sigma_{\rm I}$ is given for the Stokes I extracted with the empirical line mask and empirically accounts for systematics in the line profiles; see Section 4), with respect to the unpolarized continuum, $I_{\rm C}$. The longitudinal magnetic field, estimated from our sequences of spectra, is given in column 5. In column 6, we list the RVs measured by fitting a Gaussian function to the Stokes I LSD profiles. We adopt a conservative 1σ uncertainty of 5 m s^{-1} on the RVs. Finally, the rotational cycles listed in column 7 are computed using the reference time BJD = 2458651.993 (corresponding to the mid-transit of AU Mic b on 2019 June 19) and a rotation period of 4.86 d.

BJD [2457000+]	S/N	$\sigma_{\rm I}$ ($10^{-4} I_{\rm C}$)	$\sigma_{\rm V}$ ($10^{-4} I_{\rm C}$)	B_ℓ (G)	RV (m s^{-1})	Cycle
1744.8212	708	4.10	1.41	−43.9 ± 3.1	59.5	0.10
1750.7542	740	4.27	1.60	40.6 ± 3.7	−18.2	1.32
1751.7453	753	4.07	1.47	31.3 ± 3.2	−52.4	1.53
1752.7898	740	4.11	1.39	48.6 ± 2.9	27.9	1.74
1758.7288	678	4.13	1.36	16.2 ± 2.8	51.3	2.96
1759.8053	617	4.10	1.44	15.9 ± 3.2	69.2	3.18
1760.7278	549	4.10	1.67	48.5 ± 3.7	−29.6	3.37
1761.7305	736	4.18	1.40	24.8 ± 2.9	−87.2	3.58
1762.7315	724	4.09	1.31	52.6 ± 2.7	−2.9	3.79
1764.7571	734	4.10	1.75	23.6 ± 3.9	34.5	4.20
1765.7694	739	3.98	1.44	34.4 ± 3.2	−39.8	4.41
1769.7438	742	4.13	1.41	32.6 ± 3.1	22.1	5.23
1770.7407	678	4.07	1.56	33.4 ± 3.4	−41.6	5.43
1771.7212	664	4.04	1.45	16.4 ± 3.1	−55.8	5.64
1772.7416	629	4.17	1.57	47.2 ± 3.4	19.4	5.85
1787.7155	548	4.07	1.54	−4.7 ± 3.2	28.3	8.93
1788.7045	569	4.04	1.49	4.2 ± 3.3	41.3	9.13
1789.7367	623	4.02	1.38	82.5 ± 3.2	−32.6	9.34
1790.7010	643	4.08	1.66	12.4 ± 3.6	−90.1	9.54
1791.6983	639	4.05	1.35	40.3 ± 2.8	2.1	9.75
1792.6976	667	4.04	1.50	−24.3 ± 3.1	19.1	9.95
1796.6859	569	4.03	1.73	43.7 ± 3.6	−13.5	10.77
1797.7318	567	4.35	1.70	−48.0 ± 3.7	19.7	10.98
1798.6873	609	4.03	1.53	69.5 ± 3.5	27.0	11.18
1799.6883	559	4.11	1.68	70.0 ± 3.9	−10.3	11.39
1800.6896	724	4.06	1.40	8.8 ± 3.0	−46.2	11.60
1801.6873	703	4.12	1.55	44.3 ± 3.2	0.0	11.80

2 OBSERVATIONS AND DATA REDUCTION

AU Mic was observed between 2019 September 18 and November 14 using the nIR spectropolarimeter and high-precision velocimeter SPIRou at the CFHT atop MaunaKea, Hawaii (Donati et al. 2018, 2020). Our data set consists of 27 spectropolarimetric observations collected at a rate of one polarization sequence (i.e. four individual exposures taken at different orientations of the polarimeter retarders) per night during CFHT bright time periods. All observations were obtained in average seeing conditions (median seeing of ∼1 arcsec) and under a median airmass of 1.6. The full journal of observations is given in Table 1.

Data reduction is carried out using a version of the ESPaDOnS and NARVAL reduction pipeline (Libre-ESpRIT, Donati et al. 1997), adapted for SPIRou observations (see Donati et al. 2020). The subexposures within each polarization sequence are individually extracted using the method described in Horne (1986), and corrected for the blaze function, estimated from flat-field exposures collected prior to the observations. The individual subexposures are then combined into unpolarized (Stokes I) and circularly polarized (Stokes V) spectra, in a way to remove systematics in circular polarization

Downloaded from https://academic.oup.com/mnras/article/502/1/188/6027693 by CNRS - ISTO user on 02 February 2021

Table 2. Stellar properties of AU Mic used in this study. In particular, the stellar inclination, $i_{\rm rot}$, is assumed equal to the inclination $i_{\rm orb}$ of the planet orbit reported in P20 and consistent with the rotation-orbit alignment recently reported (see Martioli et al. 2020; Palle et al. 2020; Hirano et al. 2020). Note that ZDI reconstructions are performed assuming a stellar inclination of $i_{\rm ZDI} = 80^\circ$ (see Section 4). Note that our estimate of $v\sin i_{\rm rot}$ is consistent with the value reported in Scholz et al. (2007) and Weise et al. (2010).

Parameter	Value	Reference
Distance	9.7248 ± 0.0046 pc	Gaia Collaboration et al. (2018)
$T_{\rm eff}$	3700 ± 100 K	Afram & Berdyugina (2019)
Radius ($R_{\rm S}$)	0.75 ± 0.03 $R_\odot$	P20
Mass ($M_{\rm S}$)	0.50 ± 0.03 $M_\odot$	P20
$\log g$	4.39 ± 0.03	From $R_{\rm S}$ and $M_{\rm S}$
Luminosity	0.09 ± 0.02 $L_\odot$	Plavchan et al. (2009)
Age	22 ± 3 Myr	Mamajek & Bell (2014)
$P_{\rm rot}$	4.86 ± 0.01 d	P20
$i_{\rm orb}$	89.5 ± 0.4°	Planet orbit inclination of P20
$v\sin i_{\rm rot}$	7.8 ± 0.3 km s^{-1}	From $R_{\rm S}$, $P_{\rm rot}$, and $i_{\rm rot} = i_{\rm orb}$

spectra at first order (Donati et al. 1997; Bagnulo et al. 2009). Telluric lines from the Earth's atmosphere are modelled and filtered from our Stokes *I* spectra with the method detailed in Artigau et al. (2014). The reduced intensity spectra exhibit peak signal-to-noise ratios (S/N) per pixel (2.28 km s^{-1} velocity bin) ranging from 548 to 753 with a median value of 678 (see Table 1).

We apply least-squares deconvolution (LSD, Donati et al. 1997) to extract average Stokes *I* and *V* profiles from our set of reduced spectra. For RV measurement and brightness reconstruction (see Sections 3 and 4), we use a weighted mask of ≈3000 atomic and molecular lines, empirically built from SPIRou observations of the M2V star Gl 15A. For the magnetic analysis (see Section 5), we use a mask of atomic lines computed from an ATLAS9 local thermodynamical equilibrium model (Kurucz 1993), assuming an effective temperature $T_{\rm eff} = 3750$ K and a surface gravity $\log g = 4.5$ (see Table 2). The final mask spans the entire SPIRou spectral range (i.e. *YJHK* bands), and contains about 3600 Zeeman-sensitive atomic lines with known Landé factor and depth relative to the continuum down to 1 per cent. The extracted Stokes *I* and *V* LSD profiles feature a mean central wavelength of 1700 nm, an effective Landé factor of 1.2, and a depth of 0.24 with respect to the continuum. As a result of Zeeman broadening affecting atomic lines much more than molecular lines, the Stokes *I* LSD profiles extracted from the atomic line list are ∼2 times broader than those extracted from the empirical mask. The wavelengths of each LSD profile are finally corrected from the Barycentric Earth RV. A similar data reduction process applied to SPIRou velocimetric observations of the inactive star Gl 699 (collected at almost the same epochs as those of AU Mic), yields a median absolute deviation about the mean of 3 m s^{-1} and a standard deviation of ∼5 m s^{-1}. We thus take 5 m s^{-1} as a conservative error bar for our RV measurements of AU Mic (including a photon noise $\sigma_{\rm ph}$ that scales with the inverse S/N and contributes from 2.1 to 2.9 m s^{-1} with a median of 2.2 m s^{-1} to the error budget).

Clear Zeeman signatures of full amplitude up to 0.4 per cent with respect to the unpolarized continuum are detected in the Stokes *V* LSD profiles (see Section 5), in good agreement with previous spectropolarimetric measurements of AU Mic in the optical domain (Berdyugina et al. 2006). For each observation, we compute the longitudinal magnetic field, B_ℓ, using the relation introduced in Donati et al. (1997). The resulting B_ℓ values, listed in Table 1, range from −48 to 83 G with a median of 33 G, and a typical 1σ uncertainty of 3.2 G. The analysis of the B_ℓ time-series is described in Section 6.

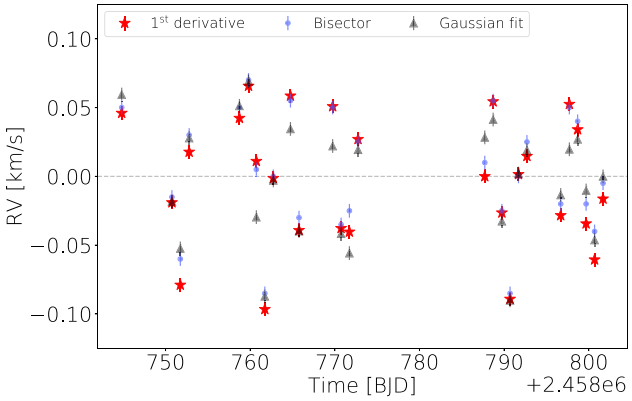

Figure 1. Median-subtracted RV time-series measured by (i) fitting a Gaussian function to the Stokes *I* LSD profiles (black triangles), (ii) computing the median value of the bisector for each observation (blue dots), and (iii) linearly adjusting the first derivative of a Gaussian function to the median-subtracted Stokes *I* LSD profiles (red stars). All RV time-series exhibit similar dispersion of 45 m s^{-1} rms.

In what follows, the rotation cycle of the star is computed from the stellar rotation period $P_{\rm rot} = 4.86$ d (P20), with the reference time BJD = 2458651.993 (called T_0 in the following), corresponding to the mid-transit of AU Mic b observed with SPIRou on 2019 June 17 (see the dedicated analysis in Martioli et al. 2020).

3 RADIAL VELOCITY ANALYSIS

3.1 RV measurement

We carry out RV measurements of AU Mic by jointly fitting a Gaussian function on top of a linear continuum (four parameters altogether) to each Stokes *I* LSD profile extracted with the empirical mask and truncated at ±31 km s^{-1} from the line centre, located at ∼4.45 km s^{-1}. The slanted continuum used in the model accounts for residual slopes in the spectrum that could bias the RV measurement process if ignored. We find that the observed profiles are relatively well fitted by a Gaussian function with a median full-width at half maximum (FWHM) of 15.8 km s^{-1} (see the RV measurements in Table 1). We consider the resulting RV time-series to be the reference one for the following RV analysis. We implemented two additional methods to measure RVs from the Stokes *I* LSD profiles. For the first one, we calculate the bisector of each line profile, corrected from residual slopes in the continuum beforehand, using the method introduced in Gray (1982) and Queloz et al. (2001). RVs are derived by computing the median bisector between 20 and 95 per cent of the full line depth (counting from the continuum). We also compute the velocity span, $V_{\rm S}$, known to be a reliable proxy of stellar activity RV signals (e.g. Queloz et al. 2001), from average velocities on the top and bottom parts of the bisector (i.e. within 20–40 and 65–95 per cent of the line depth counting from the continuum, respectively; see Section 6 for the analysis of the $V_{\rm S}$ time-series). For the second method, we scale and subtract the median Stokes *I* line, $\bar{I}$, from each LSD profile and linearly adjust the residuals with the first derivative of a Gaussian function fitted to $\bar{I}$ beforehand. The resulting RV time-series are shown in Fig. 1 and listed in Table A1. They all exhibit activity-induced fluctuations of ∼120 m s^{-1} peak-to-peak and dispersions of ∼45 m s^{-1} rms, ∼2.5 times lower than typical dispersions obtained with the High Accuracy Radial velocity Planet Searcher (HARPS) and the High-Resolution Echelle Spectrometer

Downloaded from https://academic.oup.com/mnras/article/502/1/188/6027693 by CNRS - ISTO user on 02 February 2021

(HIRES) in P20 and similar to the typical dispersion observed in nIR RV observations of AU Mic (e.g. Gagné et al. 2016, and P20, using respectively CSHELL and iSHELL spectrographs). The RV time-series exhibit median differences of $\sim$9 m s^{-1} rms between each other.

3.2 Modelling the RV time-series

We model each median-subtracted RV times-series, $\boldsymbol{V_r}$, as the sum of a planetary RV signature, $\boldsymbol{V_p}$, a stellar activity RV signal, $\boldsymbol{V_j}$, and a constant offset, V_0, such that

$$V_r(t) = V_p(t) + V_j(t) + V_0 + \epsilon(t), \quad (1)$$

where $\epsilon(t) \sim \mathcal{N}(0, \sigma(t))$, $\sigma(t)$ being the 1σ uncertainty on the data point at time t, equal to 5 m s^{-1} in our data set. Assuming a circular orbit for AU Mic b (based on the transit curve analysis of P20), the RV signal induced by the planet is simply described by

$$V_p(t) = -K_p \sin\left[2\pi \frac{t - T_0}{P_{orb}} - 2\pi\,\phi_p\right], \quad (2)$$

where K_p is the semi-amplitude of the planetary signal, P_{orb}, the orbital period of the planet and, ϕ_p, the orbital phase correction with respect to T_0/P_{orb} (T_0 being our reference time, set to the 2019 July 17 transit time, see Section 2). We assume that the planet orbital period is known from photometry ($P_{orb} = 8.46321 \pm 0.00004$ d; see P20), and that the planetary signal is perfectly phased from the mid-transit time (i.e. $\phi_p = 0$), leaving K_p as the only free parameter of the planetary model. We use Gaussian-Process Regression (GPR, Rasmussen & Williams 2006), to model the stellar activity RV signal. Similarly to the RV analysis of P20, we assume a quasi-periodic covariance kernel, k, relying on a vector of four hyperparameters, $\boldsymbol{\theta}$, and already known to accurately describe activity-induced fluctuations in RV curves for mature stars (Haywood et al. 2014; Rajpaul et al. 2015), as well as for PMS stars (e.g. Donati et al. 2016; Yu et al. 2017; Klein & Donati 2020), and given by

$$k(t_i, t_j) = \theta_1^2 \exp\left[-\frac{(t_i - t_j)^2}{\theta_2^2} - \frac{\sin^2\frac{\pi(t_i - t_j)}{\theta_3}}{\theta_4^2}\right] \quad (3)$$

where t_i is the time associated to observation i, and where θ_1 to θ_4 are respectively the amplitude, decay time, recurrence time-scale and smoothing factor of the Gaussian Process (GP). To investigate whether our model is self-consistent regarding noise statistics, we proceed as in Suárez Mascareño et al. (2020) and introduce, as an additional free model parameter, a term describing the excess of uncorrelated noise, S, accounting for potential systematics in the data beyond the assumed noise level of 5 m s^{-1} (e.g. due to stellar variability or residuals of telluric correction). The free parameters are jointly estimated by maximizing the posterior density of the model $p(\boldsymbol{\theta}, K_p, V_0, S|\boldsymbol{V_r})$, sampled using the EMCEE Markov Chain Monte Carlo (MCMC) sampler (Foreman-Mackey et al. 2013), in the Bayesian framework. We run our MCMC on 5000 iterations of 100 walkers, that is, significantly larger than the typical autocorrelation time of the chain, found to be $\sim$100 iterations in our case. The prior densities adopted for the estimation process are given in Table 3. For K_p, θ_1 and S, we use a modified Jeffreys prior (Gregory 2007), whose knee is set at the mean 1σ uncertainty on our RV data, $\bar{\sigma} = 5$ m s^{-1}, so that the prior densities are uniform (respectively, log-uniform) when the parameters are small (respectively, large) compared to $\bar{\sigma}$ (see Haywood et al. 2014). Given the low number of data points in our RV time-series, we fix the values of θ_2 and θ_4 to 100 d and 0.4 respectively (i.e. close to those quoted in P20), found to be consistent with those derived from the longitudinal field analysis[1] (see Section 6). The median and 1σ error bars on the model parameters are computed from the posterior density after removing the first 200 000 iterations (i.e. much larger than the autocorrelation time of the chain).

Table 3. Prior densities used in the Bayesian MCMC sampling of the posterior density of our RV model. Parameters written in bold are locked in the MCMC process except when otherwise indicated in the text. The knee of the modified Jeffreys prior is chosen to be the mean 1σ uncertainty on the RV measurements (in our case, $\bar{\sigma} = 5$ m s^{-1}).

Quantity	Parameter	Prior
Semi-amplitude of the planet signal	K_p	Modified Jeffreys ($\bar{\sigma}$)
Planet orbital period	P_{orb}	**8.46321 d**
Planet orbital phase	ϕ_p	**0.0**
GP amplitude	θ_1	Modified Jeffreys ($\bar{\sigma}$)
GP decay time	θ_2	**100 d**
GP recurrence period	θ_3	$\mathcal{U}$(4.5, 5.3) (d)
GP smoothing parameter	θ_4	**0.4**
Constant velocity offset	V_0	$\mathcal{U}(-100, 100)$ (m s^{-1})
Excess of uncorrelated noise	S	Modified Jeffreys ($\bar{\sigma}$)

The significance of the planet detection in the RV time-series is estimated through a Bayesian comparison of models M_1 and M_0, searching for 1 and 0 planet in the RV time-series, respectively. This is done by computing the so-called posterior odds ratio $p(M_1|V_r)/p(M_0|V_r)$, that is proportional to the Bayes factor (BF), that is, the ratio of marginal likelihoods of models M_1 and M_0 (see section 3 in Díaz et al. 2014). BF is estimated by applying the method introduced in Chib & Jeliazkov (2001) as described in Haywood et al. (2014) and Klein & Donati (2019). Following Jeffreys (1961), a BF larger than 150 (i.e. 5 in log, where log refers to the natural logarithm) would theoretically be interpreted as a fair detection of the planet in the RV time-series, while, in practice ln BF beyond 10 seems to be a more reliable threshold to claim a definite detection (see the recommandations of Nelson et al. 2020, on the interpretation of BF values).

3.3 Results

We fit the model described in Section 3.2 to the different RV time-series obtained in Section 3.1, assuming for a start that $S = 0$ m s^{-1}. The main parameters of the estimation processes are given in Table 4. The MCMC process is efficiently converging in all cases, leading to Gaussian-like posterior densities for all parameters, as illustrated in Fig. 2. The best fit to our reference RV time-series is shown in Fig. 3. In this case, we report a 3.9σ detection of a planetary signal of $K_p = 8.5^{+2.3}_{-2.2}$ m s^{-1} at the orbital period reported in P20. Consistent results are also obtained when RVs are measured using the two additional methods presented in Section 3.1 (see the results in Table 4). With BF values lying close or above the fair detection threshold (of ln BF = 5) in most cases, in particular in the reference one (first line of Table 4), we can in principle conclude that the planet RV signal is formally detected, although we caution that more data are needed to raise ln BF beyond 10 for a definite detection (Nelson et al. 2020). Leaving ϕ_p or P_{orb} as free parameters of the MCMC process yields similar results (see Table 4), further confirming that the recovered planetary signal

[1] Fixing θ_2 and θ_4 to values differing by $\sim 1\sigma$ than those reported in P20 only marginally impacts the recovered parameters of the model.

Downloaded from https://academic.oup.com/mnras/article/502/1/188/6027693 by CNRS - ISTO user on 02 February 2021

Table 4. Results of the fit to the RV time-series in case of RVs measured by (i) fitting a Gaussian function to the raw Stokes *I* LSD profiles (lines 1–5), (ii) computing the median value of the bisector (line 6), and (iii) fitting the first derivative of a Gaussian function to the median-subtracted Stokes *I* LSD profiles (line 7). For comparison purposes, we also list the results of the modelling of the RV time-series obtained by fitting a Gaussian function to the rescaled Stokes *I* LSD profiles prior to the brightness reconstruction in lines 8 and 9 (namely $\boldsymbol{I_f}$), and of the ZDI reconstruction in line 10 (see Section 4). In column 2, we give the typical RV uncertainties $\bar{\sigma}$, set to 5 m s^{-1} in all cases except for line 5 where we use instead the estimated photon noise $\sigma_{\rm ph}$. Columns 3 and 4 list the hyperparameters that maximize the posterior density (with $\pm1\sigma$ uncertainties; in all cases, θ_2 and θ_4 are respectively fixed 100 d and 0.4.). Columns 5–8 give the best estimates of $K_{\rm p}$, $\phi_{\rm p}$, $P_{\rm orb}$, and $M_{\rm p}$, computed using the stellar parameters given in Table 2 and $K_{\rm p}$. Columns 9 and 10 give the best estimates of the constant velocity offset V_0 and the excess of uncorrelated noise in our data set, *S*. All parameters are written in bold when non-optimized in the MCMC process. Finally, columns 11 and 12 indicate the rms of the residuals of the fit and the BF in favour of AU Mic b in our RV time-series.

Case	$\bar{\sigma}$ (m s^{-1})	θ_1 (m s^{-1})	θ_3 (d)	$K_{\rm p}$ (m s^{-1})	$\phi_{\rm p}$	$P_{\rm orb}$ (d)	$M_{\rm p}$ ($M_\oplus$)	V_0 (m s^{-1})	S (m s^{-1})	Rms (m s^{-1})	ln BF
Gaussian fit (reference)	5.0	47^{+11}_{-8}	4.836 ± 0.009	$8.5^{+2.3}_{-2.2}$	**0.0**	**8.46321**	$17.1^{+4.7}_{-4.5}$	2^{+20}_{-19}	**0.0**	3.0	5.6
Gaussian fit ($\phi_{\rm p}$ free)	5.0	45^{+11}_{-8}	4.836 ± 0.009	$8.2^{+2.4}_{-2.3}$	-0.03 ± 0.04	**8.46321**	$16.5^{+4.9}_{-4.7}$	3^{+20}_{-19}	**0.0**	3.1	6.3
Gaussian fit ($P_{\rm orb}$ free)	5.0	46^{+10}_{-8}	4.834 ± 0.009	8.5 ± 2.3	**0.0**	8.5 ± 0.03 d	17.1 ± 4.7	-1 ± 19	**0.0**	3.7	7.3
Gaussian fit (S free)	5.0	43^{+11}_{-8}	4.84 ± 0.01	$9.3^{+3.2}_{-3.0}$	**0.0**	**8.46321**	$18.7^{+6.5}_{-6.1}$	0^{+19}_{-18}	$6.0^{+3.8}_{-3.1}$	4.4	4.5
Gaussian fit (S free)	$\sigma_{\rm ph}$	40^{+11}_{-7}	4.84 ± 0.01	$9.3^{+3.5}_{-3.2}$	**0.0**	**8.46321**	$18.7^{+7.1}_{-6.5}$	2^{+20}_{-19}	$7.2^{+3.2}_{-2.0}$	4.3	4.1
Bisector	5.0	80^{+20}_{-15}	4.85 ± 0.01	$8.6^{+2.5}_{-2.4}$	**0.0**	**8.46321**	$17.3^{+5.1}_{-4.9}$	-13 ± 36	**0.0**	3.3	5.7
First derivative	5.0	91^{+21}_{-17}	4.85 ± 0.01	$7.8^{+2.6}_{-2.5}$	**0.0**	**8.46321**	$15.7^{+5.3}_{-5.1}$	-17 ± 40	**0.0**	3.8	4.0
Gaussian fit to $\boldsymbol{I_f}$	5.0	45^{+11}_{-8}	4.85 ± 0.01	10.1 ± 2.3	**0.0**	**8.46321**	20.3 ± 4.7	-15^{+19}_{-18}	**0.0**	3.0	7.3
Gaussian fit to $\boldsymbol{I_f}$ (S free)	5.0	38^{+11}_{-7}	4.86 ± 0.02	$10.1^{+3.1}_{-2.9}$	**0.0**	**8.46321**	$20.3^{+6.4}_{-6.3}$	-15^{+19}_{-18}	$6.4^{+3.2}_{-2.9}$	5.0	4.8
ZDI reconstruction	5.0	–	–	9.7 ± 2.5	**0.0**	**8.46321**	19.1 ± 5.1	–	–	8.7	–

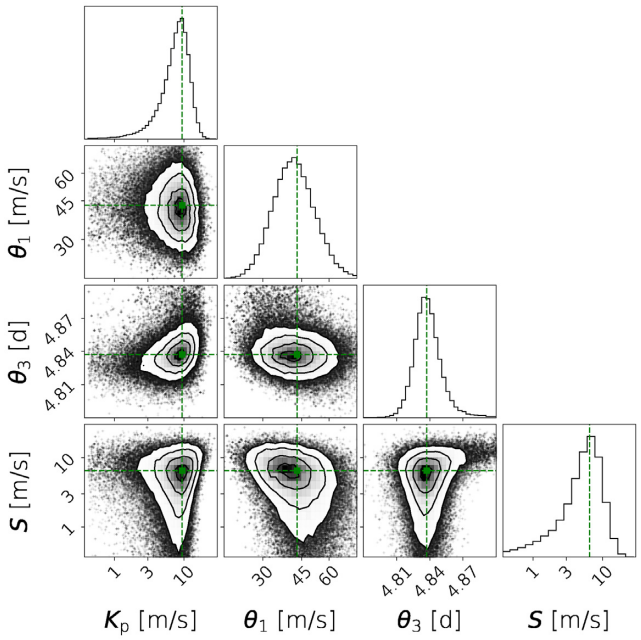

Figure 2. Posterior density resulting from the MCMC sampling of the planet and stellar activity parameters using the method described in Section 3.2. The concentric circles within each panel indicate the 1σ, 2σ, and 3σ contours of the distribution. The green dashed lines indicate the parameters that maximize the posterior density. This figure was made using the CORNER PYTHON module (Foreman-Mackey 2016). Note that the distributions of $K_{\rm p}$, θ_1 and S are shown as log -plots.

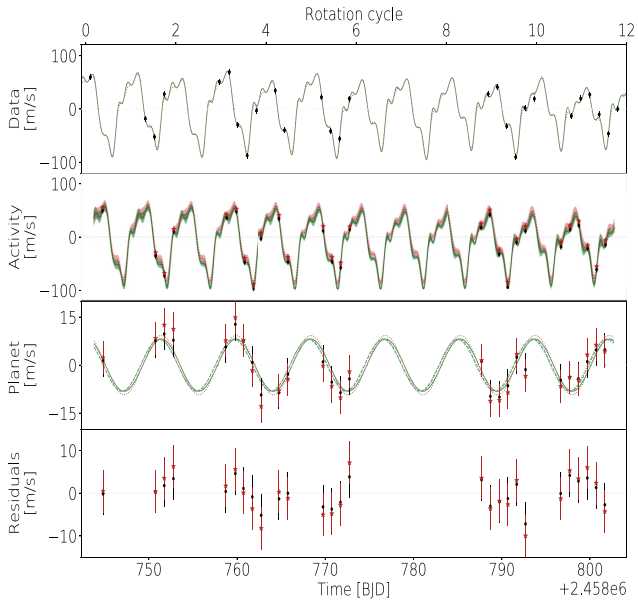

Figure 3. Best fit to the reference RV time-series. From top to bottom, we show the raw RV time-series, the stellar activity contribution, the planetary RV signature and the residuals after subtracting stellar and planetary predictions from the data. In each panel, the green solid line and red dotted line (respectively, the $\pm1\sigma$ error bands of the GP prediction in panel 2) show the best prediction of the model respectively without and with the additional uncorrelated noise *S* fitted by the MCMC process. The data points (red stars and black dots when *S* is respectively optimized in the estimation process and fixed to 0 m s^{-1}) in panels 2 and 3 and obtained by respectively subtracting the reconstructed planet and stellar activity RV signals from the raw RVs. In panel 3, the dashed and dotted green lines indicate the planet RV signal respectively obtained when $\phi_{\rm p}$ and $P_{\rm orb}$ are regarded as free parameters in the MCMC process. The residuals of the fit, shown in panel 4, exhibit respective rmss of 3.0 or 4.4 m s^{-1} when *S* is assumed to be null or fitted in the MCMC process.

is well-phased with the photometric transits reported in P20 (see also the orbit-folded time-series shown in Fig. 4). As expected from the fact that our GP is applied to the median-subtracted RV time-series, V_0 is poorly constrained by our data set, and only marginally impacts the recovered planet and stellar activity signals.

When *S* is now left as a free parameter of the model, we find $S = 6.0^{+3.8}_{-3.1}$ m s^{-1} in our reference RV time-series (see line 4 of Table 4),

Downloaded from https://academic.oup.com/mnras/article/502/1/188/6027693 by CNRS - ISTO user on 02 February 2021

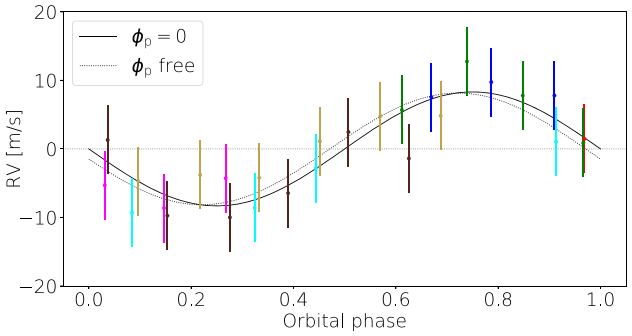

Figure 4. Activity-subtracted RV time-series (dots) folded to P_{orb} using T_0 as reference time. The subtracted activity RV signal is estimated assuming $\phi_p = 0$ and $S = 0\,m\,s^{-1}$. Data points of same colour belong to the same orbital phase. We plot in solid and dotted black lines, the planet RV signatures obtained assuming $\phi_p = 0$ and optimizing ϕ_p in the MCMC process, respectively.

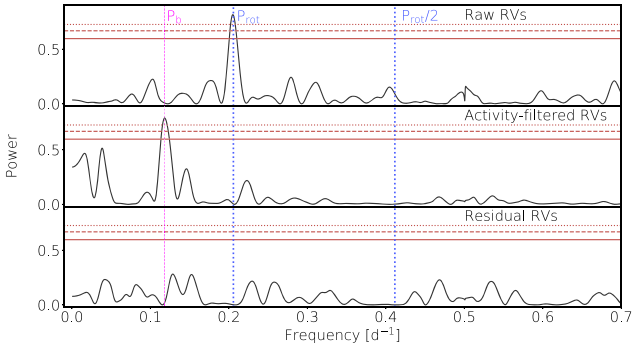

Figure 5. GLS periodograms of our reference RV time-series (top panel), the RVs obtained after subtracting the GP prediction of the stellar activity signal ($\phi_p = 0$ and $S = 0\,m\,s^{-1}$; middle panel), and the residual RVs (bottom panel). The horizontal solid, dashed, and dotted red lines indicate FAPs of respectively 10, 1, and 0.1 per cent, computed using the method described in Zechmeister & Kürster (2009) and the PYASTRONOMY PYTHON package (Czesla et al. 2019). In each panel, we indicate the frequencies corresponding to AU Mic b (P_b) and the stellar rotation period (and its first harmonic) in magenta dashed and blue dotted lines, respectively.

suggesting the presence of excess uncorrelated noise in our data.[2] However, by applying our MCMC process to synthetic RV time-series mimicking our data, we find that the low number of points in our RV time-series makes it impossible for the estimator to fully disentangle the respective contributions of the GP and of the excess uncorrelated noise, with the GP signal being partly transferred to S as a result (more information on these simulations are provided in Appendix B). As a consequence, S is likely overestimated when inferred from our limited data set.

Modelling the RV time-series obtained by computing the median value of the bisector and by fitting the first derivative of a Gaussian function to the median-subtracted Stokes I LSD profiles yields consistent estimates of the planet mass (see lines 6 and 7 of Table 4). However, the excess uncorrelated noise S takes values as high as $15\,m\,s^{-1}$ in both cases, suggesting that, in the case of active stars, both alternative methods are noisier than our reference RVs and expected to yield less accurate/reliable estimates of the planet mass.

To independently assess the reliability of the detected planet signal, we also computed a Generalized Lomb–Scargle periodogram (GLS, Zechmeister & Kürster 2009) of the RV time-series obtained by subtracting the modelled stellar activity signal from the raw RV time-series (see Fig. 5). We find a prominent peak at P_{orb} that lies slightly above the 0.1 per cent false alarm probability level (FAP; see Fig. 5). We do not find statistically significant evidence for additional planets in our data set. The GP fit to the data features slopes in the modelled RV curve reaching up to $\sim 200\,m\,s^{-1}\,d^{-1}$, with a median value of $\sim 0\,m\,s^{-1}\,d^{-1}$ over the course of our observing run, and a standard deviation of $80\,m\,s^{-1}\,d^{-1}$.

4 BRIGHTNESS IMAGING

In this section, we propose to adapt the method introduced in Petit et al. (2015) to simultaneously recover the barycentric motion due to the planet while inverting the Stokes I LSD profiles with ZDI (e.g. Semel 1989; Brown et al. 1991; Donati & Brown 1997) into a surface brightness distribution of AU Mic. ZDI proceeds through an inversion process iteratively comparing the observed LSD profiles to simulated ones from a model star whose surface brightness distribution is updated until an adequate match to the observations is reached. More specifically, ZDI carries out a maximum entropy reconstruction of the surface brightness from the adjusted LSD profiles. ZDI samples the stellar surface with a dense grid of 5000 cells from which local Stokes I profiles are computed using Unno–Rachkovsky's analytical solution to the radiative transfer equations in a Milne–Eddington atmosphere. The local profiles are Doppler shifted and weighted by the relative brightness, limb darkening and stellar inclination, before being integrated over the visible stellar hemisphere. The time-series of synthetic profiles are iteratively compared to the observed Stokes I LSD profiles until reaching the maximum entropy solution at a given level of reduced χ^2 (noted χ^2_r).

To ensure that the code robustly and efficiently converges toward the maximum entropy solution, we start by correcting residual slopes with a linear fit to the extreme profile wings (as done when deriving RVs from a Gaussian fit to the LSD profiles, see Section 3.1), so that observations optimally match modelled profiles in the continuum; we also homogenize (as usual in ZDI) the equivalent widths of all LSD profiles and truncate them at $\pm 18\,km\,s^{-1}$ from the line centre. Although AU Mic's axial inclination is likely close to 90° (see Table 2), we impose a stellar inclination of $i_{zdi} = 80°$ in the reconstruction, in order to prevent north–south degeneracy throughout the inversion process. From the stellar radius, rotation period, and stellar inclination (assumed equal to the inclination of the planet orbit) listed in Table 2, we find a projected rotational velocity $v \sin i_{rot} = 7.8 \pm 0.3\,km\,s^{-1}$, consistent with the width of the observed profiles and the value reported in Weise et al. (2010). Finally, we assume a linear limb-darkening law with a coefficient of 0.2 (as in P20).

In stars like AU Mic where the intrinsic profile at the surface of the star significantly contributes to the width of the observed LSD profile (as a result of the moderately low $v \sin i_{rot}$ of $7.8\,km\,s^{-1}$), one has to ensure that the imaging code concentrates on modelling the profile variations rather than the profiles themselves (e.g. Hébrard et al. 2016). In that aim, we first perform a maximum entropy reconstruction of the observed $\boldsymbol{I}$ profiles with ZDI, which yields an initial set of synthetic profiles $\boldsymbol{I_s}$. We then correct the observed profiles by subtracting from $\boldsymbol{I}$ the median difference between $\boldsymbol{I}$ and $\boldsymbol{I_s}$, and repeat the procedure until the median difference between $\boldsymbol{I}$ and $\boldsymbol{I_s}$ is flat.

[2] A consistent value of $S = 7.2^{+3.2}_{-2.0}\,m\,s^{-1}$ is obtained when using the photon noise alone as the formal RV uncertainty rather than the conservative $5\,m\,s^{-1}$ assumed in this study (see line 5 of Table 4).

Downloaded from https://academic.oup.com/mnras/article/502/1/188/6027693 by CNRS - ISTO user on 02 February 2021

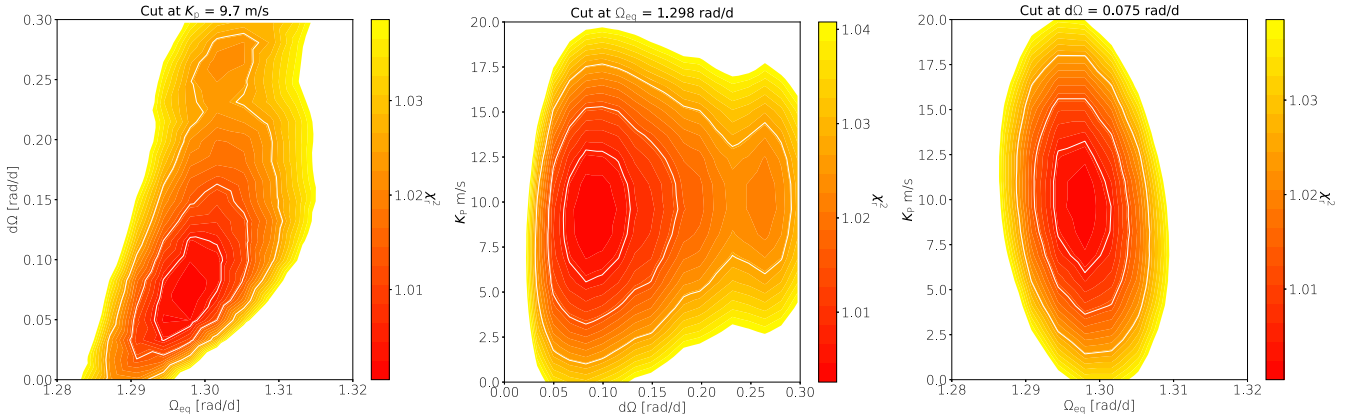

Figure 6. 2D cuts of the 3D χ^2_r map obtained by performing brightness reconstructions of $\boldsymbol{I_f}$ for a range of (Ω_{eq}, dΩ, K_p). From right to left: variations of χ^2_r in the (Ω_{eq}, dΩ) space at $K_p = 9.7\,m\,s^{-1}$, in the (K_p, dΩ) space at $\Omega_{eq} = 1.289\,rad\,d^{-1}$ and, in the (Ω_{eq}, K_p) space at $d\Omega = 0.075\,rad\,d^{-1}$. In each panel, the 1σ, 2σ, and 3σ levels are depicted by white solid lines.

As a sanity check, we measure the RVs from our final Stokes *I* LSD profiles (called $\boldsymbol{I_f}$), found to differ from our reference RVs by no more than $4.5\,m\,s^{-1}$ rms (i.e. comparable to the estimated RV noise of $\sigma = 5\,m\,s^{-1}$). Modelling these RVs using the method described in Section 3.2 unsurprisingly yields consistent planet and stellar activity parameters with those obtained in Section 3 ($K_p = 10.1 \pm 2.3\,m\,s^{-1}$ when *S* is assumed to be null, and $K_p = 10.1^{+3.1}_{-2.9}\,m\,s^{-1}$ otherwise, with $S = 6.4^{+3.2}_{-2.9}\,m\,s^{-1}$; see lines 8 and 9 of Table 4). This confirms that our final set $\boldsymbol{I_f}$ of LSD profiles retains the original time-dependent content, and that the profile distortions caused by surface features were mostly unaffected by our procedure.

Following Petit et al. (2015), we reconstruct the surface brightness of the star with ZDI at the same time as the main planet orbital parameter, K_p. Moreover, we simultaneously include the modelling of surface differential rotation (DR) as described in Donati et al. (2000) and Petit, Donati & Collier Cameron (2002), to ensure a fully consistent analysis of our observations. In practice, DR is assumed to be solar like, with the rotation rate $\Omega(\theta)$ at the surface of the star, given by

$$\Omega(\theta) = \Omega_{eq} - (\cos\theta)^2\,d\Omega, \quad (4)$$

where θ is the colatitude, Ω_{eq}, the equatorial rotation rate and, dΩ, the difference in rotation rate between the pole and the equator. The planetary signal is modelled using equation (2) and assuming that $\phi_p = 0$, which leaves K_p as the only unknown planet parameter.

We carry out brightness reconstructions of $\boldsymbol{I_f}$ for a wide range of DR and planet parameters. For each value of the parameters in the grid, (K_p, Ω_{eq}, dΩ), the reduced Stokes *I* LSD profiles are corrected from the barycentric motion induced by the planet using equation (2), and, then, reconstructed with ZDI for a given amount of information at the surface of the star (i.e. a given amount of spot coverage). Following Press et al. (1992), we derive the best parameters by fitting a 3D paraboloid to the resulting χ^2 map around the minimum, and compute the 1σ error bars on each parameter from the curvature of the modelled paraboloid. Note that the optimal parameters and the associated error bars no more than marginally depend on the level of spot coverage adopted for ZDI reconstructions.

We find that $\Omega_{eq} = 1.298 \pm 0.003\,rad/d$, $d\Omega = 0.075 \pm 0.031\,rad\,d^{-1}$, and $K_p = 9.7 \pm 2.5\,m\,s^{-1}$ provides the best reconstruction (see the 2D cuts shown in Fig. 6). The DR parameters are consistent with a solar-like DR, with rotation periods of 4.84 ± 0.01 d at the equator and 5.10 ± 0.15 d at the pole (hence a difference of $\Delta P_{rot} = 0.26 \pm 0.15$ d between the pole and the equator; note that the solid-body rotation is ruled out at 2σ). K_p is consistent within the error bars with the value obtained from the our GP modelling of Section 3.3. The reconstructed brightness map at the best planet and DR parameters is shown in Fig. 7 and the corresponding best ZDI fit is shown in Fig.8. It features a spot coverage of 1.4 per cent, with almost equal proportions of dark and bright surface features divided into two distinct groups on each side of the star. Note that surface inhomogeneties other than brightness variations (e.g. small-scale magnetic fields), may also generate similar profile variations; we come back on this point in Section 7.

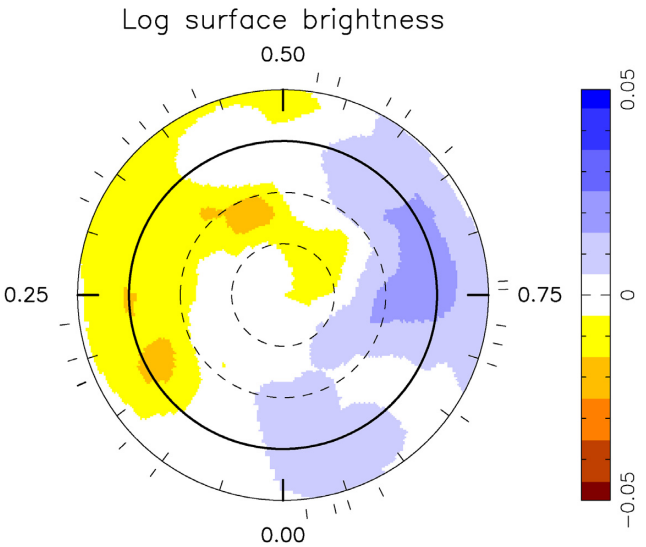

Figure 7. Flattened polar view of the surface brightness of AU Mic. The colour scale depicts the logarithm of the surface brightness (relative to the quiet photosphere), with blue/brown regions standing for bright/dark features. The black circles indicate the stellar equator (bold line) and the −30°, 30°, and 60° parallels (dashed lines). Ticks around the star mark the spectropolarimetric observations of the star.

To double check that the planet signature evidenced through our 3D paraboloid fit is truly present in the RV data, we compute the stellar activity RV signal that corresponds to our optimum maximum entropy brightness map, and use it to filter stellar activity from our reference RV curve. To achieve this, we generate synthetic Stokes

Downloaded from https://academic.oup.com/mnras/article/502/1/188/6027693 by CNRS - ISTO user on 02 February 2021

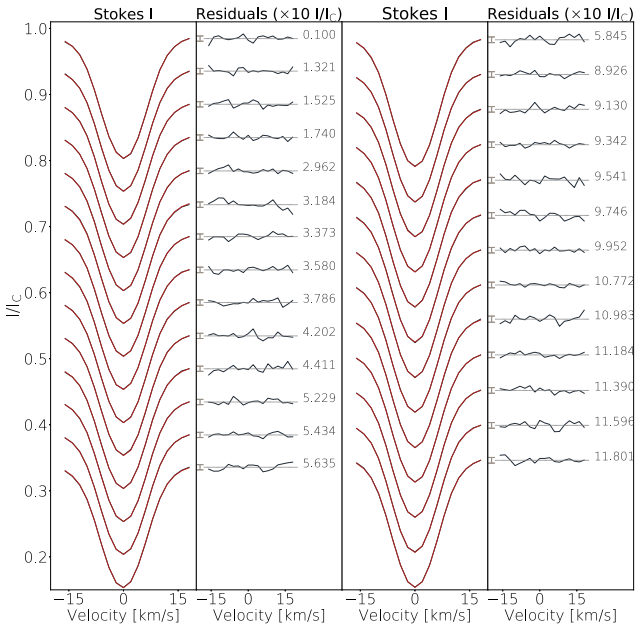

Figure 8. Panels 1 and 3: best ZDI fit (red solid lines) to the observed Stokes *I* LSD profiles (black solid lines) computed with the empirical line mask. Panels 2 and 4: residual of fit in unit of $10 \times I/I_C$. The $\pm 1\sigma$ error bar (in unit of $10 \times I/I_C$) and corresponding rotational cycle are indicated on both sides of each residual profile.

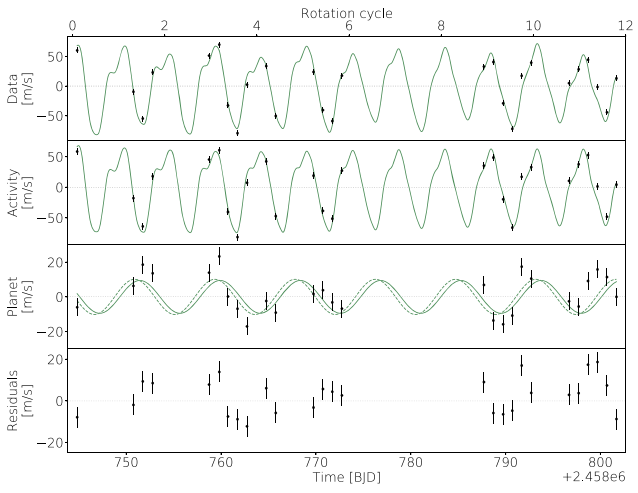

Figure 9. Same as Fig. 3, but, this time, using the maximum entropy brightness reconstruction of the star to generate the stellar activity RV curve. The solid and dashed lines in panel 3 show the recovered planet RV signatures when $\phi_p = 0.0$ and when ϕ_p is a free parameter of the model, respectively. The rms of the residuals is $9\,\mathrm{m\,s^{-1}}$.

I profiles (assuming $K_p = 0.0\,\mathrm{m\,s^{-1}}$ and the best DR parameters obtained from the ZDI reconstruction), whose RVs are subtracted from the observed RV time-series (here, the RVs measured from $\boldsymbol{I_f}$). We then fit the planetary model of equation (2) to the activity-subtracted RVs using a least-squares estimator. The best fit to the data is shown in Fig. 9. The dispersion in the residuals is $9\,\mathrm{m\,s^{-1}}$ rms, that is, ∼3 times larger than when the stellar activity is modelled with GP. This is expected as GPs are, by nature, more flexible than the current version of ZDI, and thereby capable of fitting the temporal evolution of RV curves as a result of intrinsic variability, whereas ZDI can only model that caused by DR and not that from temporal evolution of surface features. Unsurprisingly, we obtain that $K_p = 9.5 \pm 2.5\,\mathrm{m\,s^{-1}}$, fully consistent with the value obtained from the 3D paraboloid fit.[3]

5 MAGNETIC ANALYSIS

We use ZDI to perform simultaneous maximum-entropy reconstructions of the relative brightness and large-scale magnetic field at the surface of AU Mic from the observed Stokes *I* and *V* LSD profiles, extracted using the mask of atomic lines presented in Section 2. ZDI decomposes the large-scale magnetic field vector into its toroidal and poloidal components, expressed as weighted sums of spherical harmonics (Donati et al. 2006). The reconstruction process is similar to that described in Section 4, except that we now also compute synthetic Stokes *V* profiles, using again the Unno–Rachkovsky's analytical solution to the polarized radiative transfer equations, which takes both local brightness and magnetic field into account. In order to deal with the strong broadening of the Zeeman signatures in the observed Stokes *I* and *V* LSD profiles, we assume that a fraction *f* of each cell (constant over the star) includes magnetic fields of intensity *B*/*f*, whereas the rest of the cell is free of magnetic field, so that the large-scale magnetic flux over the cell is equal to *B*.

Using the same stellar parameters as for ZDI, we first invert the Stokes *V* time-series alone, pushing the spherical harmonic expansion to degree $l = 7$, given the relatively low $v \sin i_{rot}$ of the star (e.g. Morin et al. 2008). Assuming solid-body rotation, we find that $P_{rot} = 4.80 \pm 0.01$ d minimizes the χ^2_r of the reconstruction, lower than the photometric rotation period of AU Mic reported in P20. We then perform combined brightness and magnetic inversions of the observed LSD profiles and find that $f = 0.2$ reproduces best the Stokes *I* and *V* time-series down to a unit χ^2_r for both Stokes *I* and *V* profiles, starting from values of 2.8 and 11.8, respectively.

The maximum-entropy fit to the observed Stokes *I* and *V* LSD profiles is given in Fig. 10 and the corresponding brightness and large-scale magnetic maps are shown in Fig. 11. As expected, the recovered brightness map is similar to that reconstructed from our previous series of Stokes *I* LSD profiles (see Section 4 and Fig. 7). For the magnetic map, we find an average large-scale magnetic flux at the surface of the star of 475 G, and featuring a dipole of 450 G tilted at 19° to the rotation axis towards phase 0.18. The reconstructed field is found to be mainly poloidal and axisymmetric, with the poloidal component enclosing 78 per cent of the derived magnetic energy, 65 per cent of which in axisymmetric modes. The filling factor we obtain ($f = 0.2$) means that a magnetic field of ∼2.4 kG is present on ∼20 per cent of the stellar surface, consistent with the average strength of the magnetic field measured from the Zeeman broadening of unpolarized lines (Saar 1994; Reiners 2012; Shulyak et al. 2017; Moutou et al. 2017). Although the dipole is the dominant component of the reconstruction, we find that quadrupolar, octupolar, and smaller scale structures enclose a significant fraction of the total magnetic energy budget (respectively, 8, 9, and 15 per cent).

From the time-series of Stokes *V* LSD profiles alone, we estimate the stellar DR using the method introduced in Section 4. ZDI reconstructions are carried out for a range of (Ω_{eq}, $d\Omega$), leading to the 2D χ^2_r map shown in Fig. 12, from which we estimate the DR parameters with error bars using a 2D-paraboloid fit (see Donati, Collier Cameron & Petit 2003). We find that $\Omega_{eq} = 1.344$

[3]To empirically take into account the excess dispersion in the RV residuals, error bars on K_p were scaled up by $\sqrt{\chi^2_r} \approx 9/5 = 1.8$

Downloaded from https://academic.oup.com/mnras/article/502/1/188/6027693 by CNRS - ISTO user on 02 February 2021

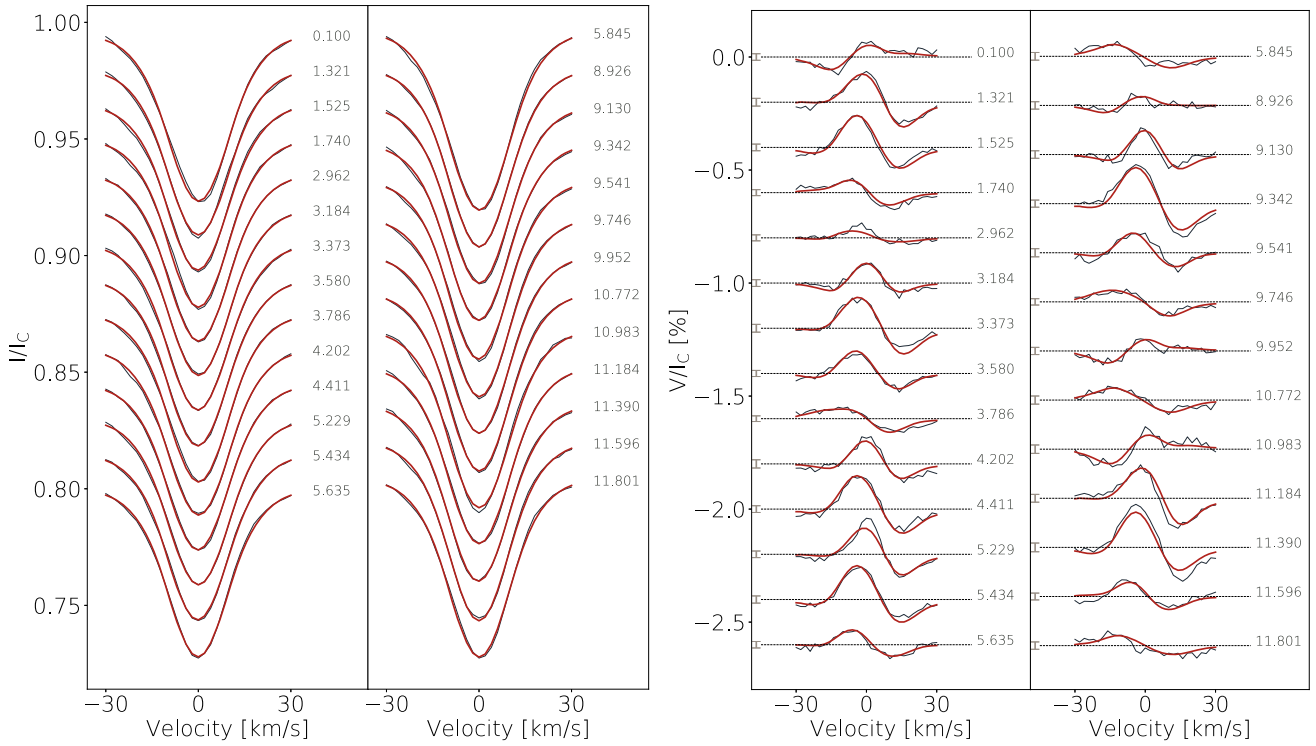

Figure 10. Best fit to the observed Stokes *I* (left-hand panel) and Stokes *V* (right-hand panel) LSD profiles. The figure elements are the same as in Fig. 8. The $\pm 1\sigma$ error bars are indicated to the left of each Stokes *V* profile.

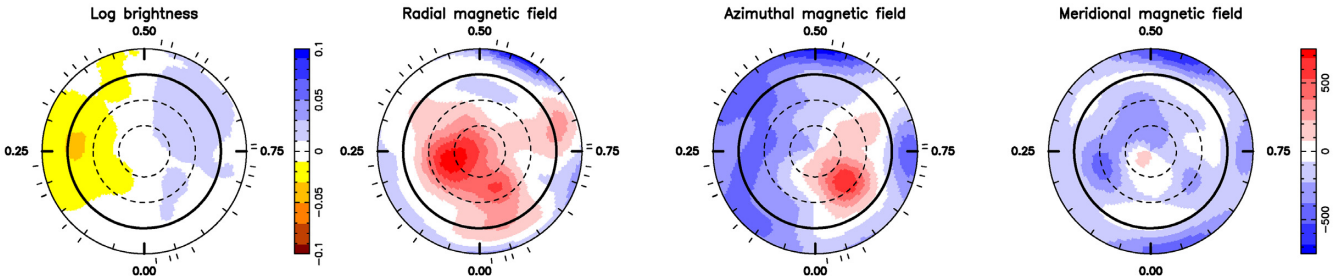

Figure 11. Logarithmic brightness (left-hand panel) and radial, azimuthal, and meridional components of the large-scale magnetic field (respectively, panels 2–4) at the surface of AU Mic. Each panel is a flattened polar view featuring the same symbols and notations as Fig. 7. Magnetic fluxes are expressed in G.

$\pm$ 0.002 rad d^{-1} and dΩ = 0.167 $\pm$ 0.009 rad d^{-1} minimizes the magnetic information at the surface of AU Mic. This implies that the rotation period of the large-scale field varies from 4.675 $\pm$ 0.006 d, around the equator, to 5.34 $\pm$ 0.05 d, at the pole (hence a difference of $\Delta P_{\rm rot} = 0.66 \pm 0.05$ d).

6 ACTIVITY INDICATORS

Optical chromospheric lines such as Hα- and Ca H&K are well-known proxies of stellar activity RV signals (e.g. Bonfils et al. 2007; Boisse et al. 2009; Gomes da Silva et al. 2011) and correlate generally well with the topology of large-scale magnetic field at the stellar surface (e.g. Hébrard et al. 2016). In the nIR, only a couple of chromospheric lines have been identified as potential probes of stellar activity at the photospheric level (e.g. He I 1083 nm and Paβ; Zirin 1982; Short & Doyle 1998), even if the way they are connected to the photosphere or transition region in low-mass stars remains unclear (e.g. Sanz-Forcada & Dupree 2008; Schmidt et al. 2012; Schöfer et al. 2019; Moutou et al. 2020). Here, we propose to compute indices based on He I triplet (1083 nm), Paβ (1282 nm), and Brγ (2165 nm). Each telluric-corrected Stokes *I* spectrum is divided by the median spectrum, in the stellar rest frame. The activity indices are computed by taking the average of each median-divided spectrum in intervals centred on the lines of interest[4] (i.e. between 1082.82 and 1083.1 nm for He I, 1281.72 and 1281.9 for Paβ, and 2165.32 and 2165.72 for Brγ). For each observation the error bars are computed from the average dispersion within 0.5 nm wide windows at each side of the lines of interest (see the values listed in Table A1). No flare is detected in the time-series of chromospheric indicators.

The small-scale magnetic flux has been shown to be an excellent proxy of stellar activity RV signals in the case of the Sun (Haywood et al. 2016, 2020). The temporal changes of this quantity are closely

[4]Each chromospheric activity index defined here is thus equal to $1 + \eta$, where $\eta = \delta f_{\rm l}/f_{\rm c}$, where $\delta f_{\rm l}$ is the difference of flux relative to the median value, and, $f_{\rm c}$, the flux of the continuum in the considered wavelength domain.

Downloaded from https://academic.oup.com/mnras/article/502/1/188/6027693 by CNRS - ISTO user on 02 February 2021

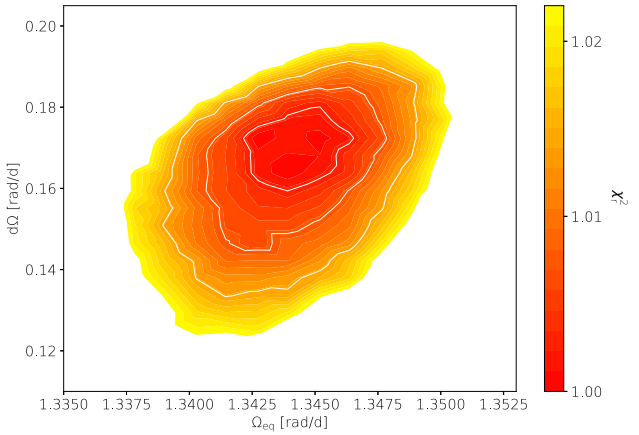

Figure 12. χ^2_r as a function of the DR parameters Ω_{eq} and dΩ derived from ZDI modelling of our time-series of Stokes *V* LSD profiles. Similarly to Fig. 6, white solid lines indicate 1σ, 2σ, and 3σ contours around the minimum χ^2_r.

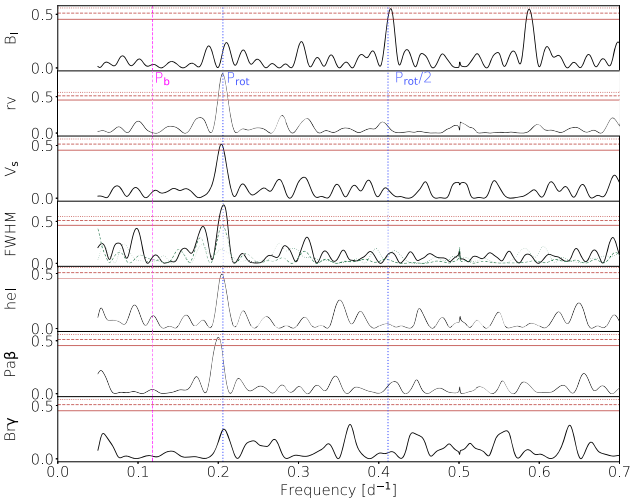

Figure 13. From top to bottom: GLS periodograms of B_ℓ, RV, $v\sin i_{rot}$, FWHM, He I, Paβ, and Brγ. Symbols are as for Fig. 5, except for FAPs that are computed at 0.3, 0.1, and 0.03. In panel 4, the green dashed and dotted lines show the GLS periodograms of the time-series of FWHMs of the profiles computed with the atomic and empirical line masks described in Section 2 (and respectively corresponding to the Stokes *I* profiles shown in Figs 8 and 10).

linked to those of the broadening of Zeeman-sensitive lines. In a way similar to that described in Section 2, we apply LSD to our reduced set of spectra but, this time, with a mask including the ∼700 lines with Landé factors larger than 1.5. We then measure the FWHM of each profile by modelling it by the sum of a Gaussian function and a linear continuum slope. In what follows, we refer to this indicator as FWHM.

The GLS peridograms of the B_ℓ, RV, velocity span (V_S), FWHM, He I, Paβ, and Brγ time-series are presented in Fig. 13. Except for Brγ, whose rotational modulation is marginally detected, all activity indicators exhibit a prominent peak around P_{rot} or its first harmonic. In particular, we note that the rotational modulation in the FWHM of Stokes *I* LSD profiles increases for lines with increasing magnetic sensitivity (i.e. increasing Landé factors). For example, the profiles computed from our empirical mask, which includes a majority of molecular lines weakly sensitive to magnetic fields, shows no more than a weak modulation.

We use GP with the quasi-periodic kernel of equation (3) to independently model B_ℓ, V_S, FWHM, as well as He I- and Paβ-based indices. For the modelling of the B_ℓ time-series, all hyperparameters are optimized by the MCMC process with Jeffreys and uniform prior densities for θ_2 and θ_4, respectively. For the other time-series, we fix θ_2 to 100 d, while θ_4 is set to 1.0 for chromospheric indicators and FWHM, and optimized for the V_S time-series.[5] As for the RV analysis, we included a constant offset and an excess uncorrelated noise to the model. The resulting rotation periods and error bars are given in Table 5 (all the results of the fits are given in Table C1, while the best predictions are shown in Fig. C1).

We find that $P_{rot} = 4.83 \pm 0.02$ d describes best the rotational modulation of the B_ℓ time-series. This value is consistent with that obtained from the RV analysis, confirming that B_ℓ is a reliable proxy of stellar rotation periods (Donati et al. 2006; Hébrard et al. 2016). The same applies to V_S and FWHM, which appear modulated at rotation periods of $4.89^{+0.04}_{-0.02}$ and 4.84 ± 0.04 d, respectively. The modelling of the chromospheric indices yields respective periods of $4.87^{+0.06}_{-0.05}$ and $4.99^{+0.11}_{-0.09}$ d for He I and Paβ, both compatible with the rotation period of the star.

The time-series of activity indicators are phase-folded at $P_{rot} = 4.86$ d in Fig. 14. At the first order, the chromospheric indicators appear well correlated with B_ℓ and anticorrelated with RV. In particular, the longitudinal field appears best correlated with Paβ, with a maximum around phase 0.3, when the magnetic pole is pointing toward the observer. In contrast, the He I flux is maximum around phase 0.6, when the magnetic equator faces the observer (the magnetic dipole is tilted at 19° to the rotation axis; see Fig. 11), emphasizing the fact that He I is mostly observed at low latitudes. We also find that the FWHM is remarkably phased with RVs, suggesting that the small-scale magnetic field and the regions of the stellar disc responsible for the RV fluctuations are closely located.

In order to compare the ability of the indicators to model stellar activity RV signals, we compute the Pearson correlation coefficient, ρ, between each time-series of indicators and the planet-subtracted RVs measured in Section 3.1. The resulting correlation plots are shown in Fig. 15 (see also all the correlations in Fig. C2). The RV time-series is best correlated with V_S and FWHM, confirming that both the velocity span and the small-scale magnetic flux are reliable proxies of stellar activity for moderate-to-fast rotators in the nIR. We also observe a moderate anticorrelation between RVs and He I, suggesting that this indicator describes relatively well the variations induced by non-axisymmetric features on the line profiles. Although we find that our RVs are well phased with a simple sine fit to the B_ℓ time-series (see the top panel of Fig. 14), higher frequency structures in B_ℓ reduce the correlation with the RVs. No significant correlation is identified between RVs and Paβ, that appear more sensitive to magnetic structures located at higher latitudes. Finally, Brγ has no visible modulation and appears to be a poor indicator of stellar activity in the case of AU Mic.

[5] θ_4 is set to 1.0 when modelling the chromospheric activity indicators, whereas 0.4 was used in the case of the RVs. This is because active regions at the stellar surface produce RV signatures evolving about twice faster with time than their counterparts in the curves of activity proxies. The recurrence time-scale of the GP (θ_3) is found to be marginally affected by variations of the order of 0.1 in θ_4.

Downloaded from https://academic.oup.com/mnras/article/502/1/188/6027693 by CNRS - ISTO user on 02 February 2021

Table 5. Best rotation period (line 1) from GP modelling of the different activity indicators described in Section 6, and Pearson correlation coefficient (ρ, line 3) of these indicators with the planet-subtracted RVs. The last column indicates the rotation period obtained from the ZDI modelling of the Stokes *V* LSD profiles (see Section 5). For comparison, the DR parameters estimated from the time-series of Stokes *I* and *V* profiles yield respective rotation periods of 4.84 ± 0.01 and 4.675 ± 0.006 d at the stellar equator, and 5.10 ± 0.15 and 5.34 ± 0.04 d at the stellar pole.

	RVs	B_ℓ	V_S	FWHM	He I	Paβ	Stokes *V*
P_{rot}	4.84 ± 0.01 d	4.83 ± 0.02	$4.89^{+0.04}_{-0.02}$	4.84 ± 0.04	$4.87^{+0.06}_{-0.05}$	$4.99^{+0.11}_{-0.09}$	4.80 ± 0.01
ρ	–	−0.214	−0.695	0.691	−0.503	−0.281	–

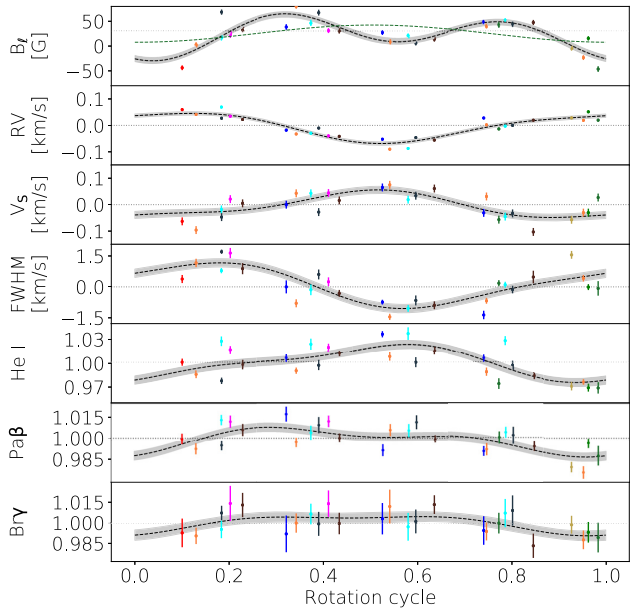

Figure 14. From top to bottom: time-series of B_ℓ RV, V_S, FWHM, He I, Paβ, and Brγ, phase-folded at a rotation period of 4.86 d. In each panel, a double sine-wave fit (with 1 harmonic) to the time-series assuming a period of P_{rot} is shown in black dashed lines (with ±1σ error bands). Similarly to Fig. 4, data points of different colours belong to different rotational cycles. In the top panel, we show the best simple sine-wave fit to the B_ℓ time-series at a rotation period of 4.86 d.

7 DISCUSSION AND CONCLUSION

In this study, we conducted a velocimetric and spectropolarimetric analysis of a data set consisting of 27 observations of AU Mic collected with SPIRou from 2019 September 18 to November 14. Using LSD, we computed average Stokes *I* and Stokes *I* and *V* profiles using two different line masks, one empirically built from a SPIRou spectrum of an early M dwarf (Gl 15A) and containing both atomic and molecular lines, and another including atomic lines with known Landé factors only. Stellar RVs are measured with a conservative 1σ uncertainty of 5 m s^{-1}, and exhibit fluctuations of up to 150 m s^{-1} peak-to-peak with an rms of 45 m s^{-1}. A third mask including lines with strongest magnetic sensitivity was also used to estimate the amount of Zeeman broadening of Stokes *I* profiles, and its modulation with time.

We carried out the search for a planet signature at AU Mic b's orbital period, assuming a circular orbit, in our RV time-series. Stellar activity and planet RV signals were jointly estimated, resulting in a 3.9σ detection of the planet-induced RV signature, implying a mass of $17.1^{+4.7}_{-4.5}$ $M_\oplus$ (i.e. 1.0 ± 0.3 M_{Nep}). Including an excess of uncorrelated noise *S* in the free parameters of the model yields a planet mass estimate of $18.7^{+6.5}_{-6.1}$ $M_\oplus$, compatible with the previous value but with a larger uncertainty. However, simulations demonstrate that the value of *S* recovered from the fit to the data is most likely overestimated in our limited data set, leading to artificially enhanced error bars on the planet mass. We thus consider that the planet mass derived assuming $S = 0$ m s^{-1} is the most reliable and robust estimate that one can retrieve from our data set.

A consistent measurement of the planet mass is independently obtained by performing a reconstruction of the surface brightness of the star with ZDI while estimating the planet parameters. In this process, the stellar activity RV signal is modelled by bright and dark features at the surface of the star. In fact, it is entirely possible that the reconstructed surface brightness inhomogeneities modulating the width of Stokes *I* profiles probe (at least partly) small-scale magnetic fields rather than brightness features. The fact that the FWHM of lines with higher magnetic sensitivity is more strongly modulated (see Fig. 13) is further evidence that the activity-induced RV signal is indeed of magnetic origin. Breaking the degeneracy between surface brightness and magnetic field would require to simultaneously model Stokes *I* LSD profiles of spectral lines with different magnetic sensitivities, so that the differences in their modulation pattern can be reliably inverted into maps of the surface brightness and small-scale magnetic field. As this approach requires a full-size study in itself, we postpone it to a forthcoming paper.

When combined with the transit radius, the planet mass yields a mean density of 1.3 ± 0.4 g cm^{-3}, comparable to that of Neptune within the 1σ error bars, which is relatively high compared to the prediction of global models of planet formation and evolution, and suggests that the planet features a high fraction of heavy elements (typically $\gtrsim$80 per cent; e.g. Mordasini et al. 2012b). AU Mic b is compared to older low-mass exoplanets with well-constrained mean density in the mass-mean density diagram shown in Fig. 16. When compared to the theoretical evolution of the mass-radius relation of sub-Neptunes of Lopez & Fortney (2014), AU Mic b is expected to be a core-dominated planet featuring an H/He envelope occupying $\gtrsim$20 per cent of the total planet mass. We also note that AU Mic b lies fairly close to the lower limit of the so-called evaporation valley (e.g. Owen & Wu 2013; Lopez & Fortney 2013; Jin et al. 2014; Jin & Mordasini 2018; Mordasini 2020). AU Mic b has an equilibrium temperature (∼600 K) and radius of the same order of the well-known evaporating sub-Neptune GJ 436 b (e.g. Bourrier et al. 2018) and may thus be in the process of loosing its H/He envelope which would lead it to cross the evaporation valley on time-scales of a few tens of Myr (Jin & Mordasini 2018). Measuring the metallicity of the planet atmosphere, as well as detecting extended exospheres of hydrogen or helium, will greatly improve our understanding of the nature of AU Mic b, its formation history, and its future evolution.

Using ZDI, we derived the surface brightness and large-scale magnetic maps of AU Mic. Cool and warm features are present in roughly equal proportions, totalling 1–2 per cent of the whole

Downloaded from https://academic.oup.com/mnras/article/502/1/188/6027693 by CNRS - ISTO user on 02 February 2021

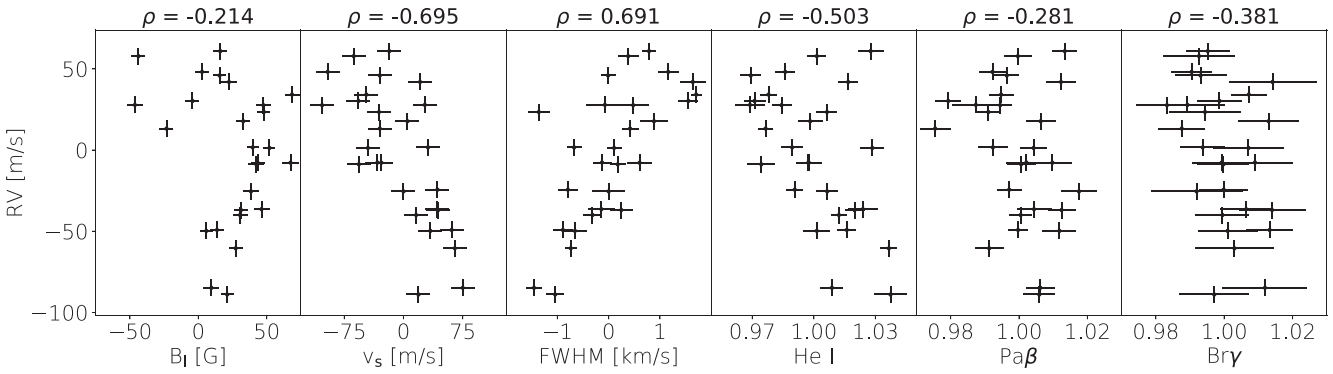

Figure 15. Correlation plots of the RV time-series (measured by fitting a Gaussian function to each Stokes *I* LSD profile) as a function of (from left to right): the longitudinal field, velocity span, FWHM, He I, Paβ, and Brγ. The Pearson correlation coefficient, ρ, is written at the top of each panel. Note that the planet signature was removed from the RVs for these curves, and before computing the correlation coefficients.

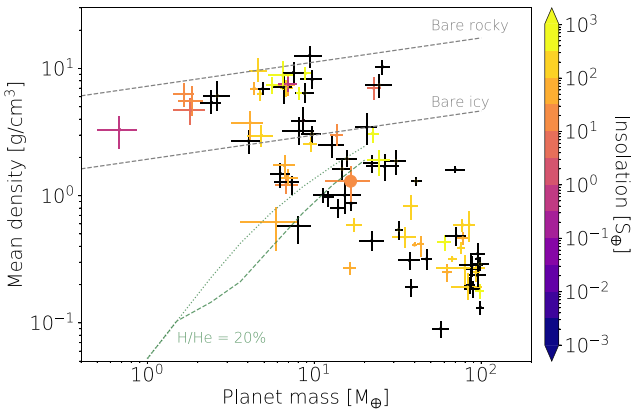

Figure 16. Mass-mean density diagram of confirmed exoplanets of mass lower than 100 $M_\oplus$ and with relaive uncertainties on the mass and the mean density lower than 33 per cent, computed from https://exoplanetarchive.ipac.caltech.edu/. The colour scale depicts the insolation of the planet (planets are plotted in black when insolation is not known). AU Mic b is indicated by the large filled circle. For comparison purposes, we plot the theoretical limits of pure icy and rocky cores (i.e. completely evaporated envelope), computed using Jin & Mordasini's (2018) relations. Green dashed and dotted lines indicate the expected density of a 100 Myr planet under AU Mic b's stellar flux hosting a 20 per cent H/He envelope assuming respectively solar and 50 times solar planet metallicities predicted from Lopez & Fortney's (2014) theoretical models. Note that all planets but AU Mic b shown in this diagram orbit stars older than 100 Myr.

stellar surface probed by ZDI. In particular, regions dominated by dark spots and warm plages are well separated at the surface of the star. We find a large-scale magnetic field of 475 G featuring a mainly poloidal and axisymmetric field dominated by a 450 G-dipole component tilted at 19° to the rotation axis. We find that the large-scale field is sheared by a surprisingly large solar-like DR of $d\Omega = 0.167$ rad/d (i.e. the equator rotates faster than the pole), about twice stronger than that observed in our brightness reconstruction and 3 times larger than that of the Sun. The discrepancy between the equatorial periods derived from the Stokes *I* and *V* profiles suggests that both methods probe different layers of the convective zone. More specifically, by combining our DR parameters, we find that $\Omega_{eq} = 0.48d\Omega + \Omega_0$, where Ω_0 is a constant (for the Sun, $\Omega_{eq} = 0.2d\Omega + \Omega_0$). This is compatible with the typical angular velocity fields of rapid rotators like AB Dor, best described with an angular rotation constant over axisymmetric cylinders (Donati et al. 2003). In this context, the magnetic field would probe layers close to the surface while dark and bright features (and the related small-scale field) are likely anchored deeper in the convective zone. We caution that this result may be impacted by the high level of temporal variability of AU Mic's activity and, therefore, needs to be validated by additional spectropolarimetric observations.

Activity indicators based on B_ℓ, V_S, He I, Paβ, Brγ, and FWHM (probing the small-scale field) were computed at each observing epoch. Except for Brγ, all time-series exhibit a clear rotational modulation. Interestingly, time-series associated with He I and Paβ are modulated with different periods, suggesting that they probe different regions of the stellar surface, He I being mostly coupled with the magnetic equator, while Paβ is more sensitive to the magnetic pole and, as such, is more correlated with B_ℓ than with RVs. Since the non-axisymmetric features reconstructed with ZDI are mostly located around the stellar equator, He I stands for a better proxy of the stellar activity RV signal than B_ℓ or Paβ. Finally, we note that both the bisector span and the small-scale magnetic field correlates best with our RV time-series, confirming their high sensitivity to stellar activity, even in the nIR.

The magnetic properties of AU Mic are relatively similar to those of the more evolved star AD Leo (see the compared stellar properties of Table 6). Both stars are located on close evolutionary tracks in the Hertzsprung-Russell (HR) diagram (see Fig. 17), and one may wonder if AU Mic will resemble AD Leo at the beginning of the MS. The evolutionary tracks of Siess et al. (2000)/Baraffe et al. (2015) predict stellar radii of 0.4/0.5 $R_\odot$ for AU Mic at the age of AD Leo (i.e. ∼100 Myr according to the stellar evolution models, consistent with literature estimates; Shkolnik et al. 2009; Tuomi et al. 2018). Assuming the conservation of stellar flux and angular momentum during the PMS phase, we predict average magnetic fields of 1.75/0.95 kG and rotation periods of 1.3/2.4 d for AU Mic at ∼100 Myr. While the expected rotation period for AU Mic in the case of the Baraffe et al. (2015) models (yielding a mass estimate for AD Leo in better agreement with observations) is comparable to that of AD Leo, the predicted field strengths are one order of magnitude larger, demonstrating that magnetic flux conservation (more or less verified in the case of fossil fields, e.g. Landstreet et al. 2007) does not apply in the case of dynamos where field amplification is mainly fuelled from the kinetic energy reservoir of the convective zone. Both stars are predicted fully and partly convective by Siess et al.

Downloaded from https://academic.oup.com/mnras/article/502/1/188/6027693 by CNRS - ISTO user on 02 February 2021

Table 6. Comparison of AU Mic and AD Leo stellar properties. Lines 7 and 8 give respectively the relative depth of the convective envelope, R_C (in unit of stellar radius, R_S), and the moment of inertia relative to $M_S R_S{}^2$, k_i, computed from Siess, Dufour & Forestini (2000) and Baraffe et al. (2015) models. The last four lines give the average intensity of the large-scale magnetic field, B_V, and the fractions of poloidal (f_{pol}), dipolar (poloidal, f_{dip}), and axisymmetric (poloidal, f_{axi}) modes of the magnetic energy reconstructed by ZDI (the two values given for AD Leo correspond respectively to the reconstructions of Morin et al. 2008; Lavail, Kochukhov & Wade 2018). The properties of AU Mic predicted at an age of 100 Myr by Siess et al. (2000)/Baraffe et al. (2015) models, assuming the conservation angular momentum, are given in column 3. Except for lines 7 and 8, the references listed in column 5 refer to AD Leo (see Table 2 for the references associated to AU Mic properties). We note that the measured mass and age of AD Leo are in better agreement with the models of Baraffe et al. (2015) than with those of Siess et al. (2000).

Parameter	AU Mic	AU Mic at 100 Myr	AD Leo	References for AD Leo
Age (Myr)	22 ± 3	100	25-300	Shkolnik, Liu & Reid (2009)
T_{eff} (K)	3700 ± 100	3750/3880	3471 ± 60	Gaidos et al. (2014)
Radius ($R_\odot$)	0.75 ± 0.03	0.39/0.53	0.402 ± 0.010	Mann et al. (2015)
Mass ($M_\odot$)	0.50 ± 0.03	0.50	0.427 ± 0.011	Mann et al. (2015)
Luminosity ($L_\odot$)	0.09 ± 0.02	0.04/0.06	0.022 ± 0.002	From T_{eff} and mass
P_{rot} (d)	4.836 ± 0.008	1.3/2.4	2.2399 ± 0.0006	Morin et al. (2008), Tuomi et al. (2018)
R_C (R_S)	1.0/0.6	0.91/0.36	1.0/0.6	Siess et al. (2000)/Baraffe et al. (2015)
k_i	0.2/0.2	0.2/0.2	0.2/0.2	Siess et al. (2000)/Baraffe et al. (2015)
B_V (G)	475	–	190-300	Morin et al. (2008)–Lavail et al. (2018)
f_{pol} (per cent)	80	–	99-90	Morin et al. (2008)–Lavail et al. (2018)
f_{dip} (per cent)	60	–	60-90	Morin et al. (2008)–Lavail et al. (2018)
f_{axi} (per cent)	65	–	90-95	Morin et al. (2008)–Lavail et al. (2018)

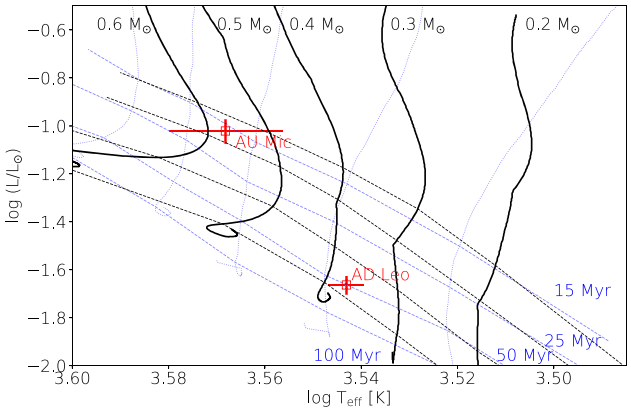

Figure 17. Location of AU Mic, and AD Leo in the HR diagram (with 1σ error bars). The PMS evolutionary tracks for masses of 0.2, 0.3, 0.4, 0.5, and 0.6 $M_\odot$ are plotted in thick black solid lines (for the models of Baraffe et al. 2015) and thin blue dotted lines (for the models of Siess et al. 2000, assuming solar metallicity and including convective overshooting). The corresponding isochrones at 15, 25, 50, and 100 Myr are plotted in black and blue dashed lines.

(2000) and Baraffe et al. (2015) models, respectively (see Table 6). While AU Mic will definitely be partly convective when reaching the MS, AD Leo lies slightly above the full-convection threshold of ∼0.35 $M_\odot$ (Baraffe et al. 1998, 2015), in the region of P_{rot}–Mass diagram where the magnetic properties of M dwarfs are known to significantly differ from those of their more massive counterparts (Donati et al. 2008; Morin et al. 2008, 2010).

Similarly, we may wonder what AU Mic looked like at the time its inner accretion disc was exhausted, that is, at a younger age of under 10 Myr. In particular, did AU Mic b have enough time to migrate within the magnetospheric cavity of its host star? In this case, the close-in planet would stand as a signpost for the location of the inner accretion disc and flag where the corotation radius lay at the time of the disc dissipation (Lin, Bodenheimer & Richardson 1996). Assuming the conservation of angular momentum, this would imply that the disc dissipation occured when AU Mic has a radius of $R_S \simeq 1\,R_\odot$, that is, at an age of about 8 Myr (according to Baraffe et al. 2015). However, the dipole field that the young AU Mic would have needed to carve a magnetospheric cavity as large as 0.066 au is significantly larger (at least 1.8 kG) than the one it now hosts, even for accretion rates as low as $10^{-10}\,M_\odot\,yr^{-1}$ (Bessolaz et al. 2008). Another option is that AU Mic b did not have enough time to migrate within the magnetospheric gap before the disc disappeared, or was trapped on its way by interactions with other planets in the system.

This study confirms the ability of SPIRou to carry out precise RV and spectropolarimetric measurements of bright nearby M dwarfs. As already demonstrated with simulations, stars with rotation periods of a few days hosting surface features evolving on significantly longer time-scales are excellent targets for high-precision RV follow-ups (Klein & Donati 2020). In the specific case of low-mass PMS stars like AU Mic, observing in the nIR rather than in the visible turns out to be a definite advantage to disentangle planet signatures from stellar activity RV signals, the latter being much weaker in this domain. These results are promising for future SPIRou observations of young stars hosting transiting planets to be observed as part of the SPIRou Legacy Survey (e.g. David et al. 2016, 2019a, b).

AU Mic b is the first close-in Neptune-sized planet younger than 25 Myr to have its inner density measured at $>3\sigma$. Given the corotation radius of the star (located at $13\,R_S = 0.044$ au), the magnetic field lines are expected to be mostly open under the effect of centrifugal forces at the distance of the planet (∼19 R_S = 0.066 au), implying that magnetic star–planet interactions should operate in the super-Alfvénic regime (Strugarek et al. 2015). Magnetohydrodynamical simulations are required to validate this conclusion and further constrain the extended magnetosphere and wind of the star, as well as its interaction with the close-in planet (e.g. Vidotto & Donati 2017; Vidotto & Bourrier 2017). We also note that the tilted large-scale magnetic field that we find to be present at the surface of AU Mic may induce a time-dependent wind (Vidotto et al. 2014), potentially responsible for the fast moving features identified in the debris disc, as discussed in Wisniewski et al. (2019).

Given the brightness of its host star, this planet is a primary candidate for an atmospheric characterization with ground-based

Downloaded from https://academic.oup.com/mnras/article/502/1/188/6027693 by CNRS - ISTO user on 02 February 2021

nIR spectrometers and upcoming space missions like the *JWST*. Additional more extensive spectropolarimetric observations of AU Mic with SPIRou, with as much as ∼100 visits, are crucially needed to accurately pin down the planet mass. These observations will also allow to bring a more precise measurement of the ellipticity of its orbit, which should help retracing the planet formation history and possible dynamical interactions with other putative planets in the system (Chatterjee et al. 2008; Jurić & Tremaine 2008). Moreover, given its low mass, AU Mic b is unlikely to be responsible for the ejection of the fast moving features in the debris debris (see the discussion in P20). Hence the interest in conducting more observation campaigns in order to search for further massive bodies whose past orbital evolution could explain the dynamical properties of these features. These observations will also allow us to confirm the surprisingly high DR found in our analysis and investigate the variability of the stellar activity and magnetic field. Finally, an even longer term spectropolarimetric monitoring of AU Mic would allow to investigate how the fractions of axisymmetric and poloidal magnetic energies and the DR parameters evolve on time-scales of 5–10 yr. These parameters are reliable proxies of solar-like magnetic cycles (see Lehmann et al. 2021) that will help confirming the 5 yr-activity cycle reported in Ibañez Bustos et al. (2019), thought to be powered by a solar-like $\alpha\Omega$-dynamo process.

ACKNOWLEDGEMENTS

This work is based on observations obtained at the CFHT which is operated from the summit of Maunakea by the National Research Council Canada, the Institut National des Sciences de l'Univers of the Centre National de la Recherche Scientifique of France, and the University of Hawaii. The observations at the CFHT were performed with care and respect from the summit of Maunakea which is a significant cultural and historic site. The observations analysed in this work were obtained with SPIRou, an international project led by Institut de Recherche en Astrophysique et Planétologie, Toulouse, France.

This project was funded by the European Research Council (ERC) under the H2020 research and innovation programme (grant agreement no. 740651 NewWorlds). We acknowledge funding from Agence Nationale de la Recherche (ANR) under contracts ANR-18-CE31-0019 (SPlaSH) and ANR-15-IDEX-02 (Origin of Life at Université Grenobles Alpes).

We warmly thank the referee for valuable comments and suggestions which helped us improving an earlier version of the manuscript.

DATA AVAILABILITY

The data underlying this article will be available in the Canadian Astronomy Data Center[6] from 2021 February 28.

REFERENCES

Afram N., Berdyugina S. V., 2019, A&A, 629, A83
Alibert Y., Mordasini C., Benz W., Winisdoerffer C., 2005, A&A, 434, 343
Artigau É. et al., 2014, in Proc. SPIE, Vol. 9149, p. 914905
Bagnulo S., Landolfi M., Landstreet J. D., Land i Degl'Innocenti E., Fossati L., Sterzik M., 2009, PASP, 121, 993
Baraffe I., Chabrier G., Allard F., Hauschildt P. H., 1998, A&A, 337, 403
Baraffe I., Homeier D., Allard F., Chabrier G., 2015, A&A, 577, A42
Baruteau C., Bai X., Mordasini C., Mollière P., 2016, Space Sci. Rev., 205, 77
Berdyugina S. V., Petit P., Fluri D. M., Afram N., Arnaud J., 2006, in Casini R., Lites B. W., eds, ASP Conf. Ser. Vol. 358, Solar Polarization 4. Boulder, Colorado, USA, p. 381
Bessolaz N., Zanni C., Ferreira J., Keppens R., Bouvier J., 2008, A&A, 478, 155
Boccaletti A. et al., 2015, Nature, 526, 230
Boccaletti A. et al., 2018, A&A, 614, A52
Boisse I. et al., 2009, A&A, 495, 959
Bonfils X. et al., 2007, A&A, 474, 293
Bourrier V. et al., 2018, A&A, 620, A147
Brown S. F., Donati J. F., Rees D. E., Semel M., 1991, A&A, 250, 463
Chatterjee S., Ford E. B., Matsumura S., Rasio F. A., 2008, ApJ, 686, 580
Chiang E., Fung J., 2017, ApJ, 848, 4
Chib S., Jeliazkov I., 2001, J. Am. Stat. Assoc., 96, 270
Crockett C. J., Mahmud N. I., Prato L., Johns-Krull C. M., Jaffe D. T., Hartigan P. M., Beichman C. A., 2012, ApJ, 761, 164
Cutri R. M. et al., 2003, 2MASS All Sky Catalog of Point Sources, http://irsa.ipac.caltech.edu/applications/Gator/
Czesla S., Schröter S., Schneider C. P., Huber K. F., Pfeifer F., Andreasen D. T., Zechmeister M., 2019, Astrophysics Source Code Library, record ascl:1906.010
Daley C. et al., 2019, ApJ, 875, 87
David T. J., Petigura E. A., Luger R., Foreman-Mackey D., Livingston J. H., Mamajek E. E., Hillenbrand L. A., 2019b, ApJ, 885, L12
David T. J. et al., 2016, Nature, 534, 658
David T. J. et al., 2019a, AJ, 158, 79
Donati J.-F. et al., 2018, SPIRou: A NIR Spectropolarimeter/High-Precision Velocimeter for the CFHT. Springer International Publishing, Cham, p. 107
Donati J. F., Brown S. F., 1997, A&A, 326, 1135
Donati J. F., Collier Cameron A., Petit P., 2003, MNRAS, 345, 1187
Donati J. F., Landstreet J. D., 2009, ARA&A, 47, 333
Donati J. F., Mengel M., Carter B. D., Marsden S., Collier Cameron A., Wichmann R., 2000, MNRAS, 316, 699
Donati J. F., Semel M., Carter B. D., Rees D. E., Collier Cameron A., 1997, MNRAS, 291, 658
Donati J. F. et al., 2006, MNRAS, 370, 629
Donati J. F. et al., 2008, MNRAS, 390, 545
Donati J. F. et al., 2014, MNRAS, 444, 3220
Donati J. F. et al., 2016, Nature, 534, 662
Donati J. F. et al., 2020, MNRAS, 498, 5684
Díaz R. F., Almenara J. M., Santerne A., Moutou C., Lethuillier A., Deleuil M., 2014, MNRAS, 441, 983
Foreman-Mackey D., 2016, J. Open Source Softw., 1, 24
Foreman-Mackey D., Hogg D. W., Lang D., Goodman J., 2013, PASP, 125, 306
Gagné J. et al., 2016, ApJ, 822, 40
Gaia Collaboration et al., 2018, A&A, 616, A1
Gaidos E. et al., 2014, MNRAS, 443, 2561
Gomes da Silva J., Santos N. C., Bonfils X., Delfosse X., Forveille T., Udry S., 2011, A&A, 534, A30
Gray D. F., 1982, ApJ, 255, 200
Gregory P. C., 2007, MNRAS, 381, 1607
Haywood R. D. et al., 2014, MNRAS, 443, 2517
Haywood R. D. et al., 2016, MNRAS, 457, 3637
Haywood R. D. et al., 2020, preprint (arXiv:2005.13386)
Hill C. A., Folsom C. P., Donati J. F., Herczeg G. J., Hussain G. A. J., Alencar S. H. P., Gregory S. G., Matysse Collaboration, 2019, MNRAS, 484, 5810
Hirano T. et al., 2020, ApJ, 899, L13
Horne K., 1986, PASP, 98, 609
Hébrard É. M., Donati J. F., Delfosse X., Morin J., Moutou C., Boisse I., 2016, MNRAS, 461, 1465
Ibañez Bustos R. V., Buccino A. P., Flores M., Martinez C. I., Maizel D., Messina S., Mauas P. J. D., 2019, MNRAS, 483, 1159
Jeffreys H., 1961, Theory of Probability, third edn. Oxford, Oxford, England
Jin S., Mordasini C., 2018, ApJ, 853, 163

[6] https://www.cadc-ccda.hia-iha.nrc-cnrc.gc.ca/

Downloaded from https://academic.oup.com/mnras/article/502/1/188/6027693 by CNRS - ISTO user on 02 February 2021

Jin S., Mordasini C., Parmentier V., van Boekel R., Henning T., Ji J., 2014, ApJ, 795, 65
Johns-Krull C. M. et al., 2016, ApJ, 826, 206
Jurić M., Tremaine S., 2008, ApJ, 686, 603
Kalas P., Liu M. C., Matthews B. C., 2004, Science, 303, 1990
Klein B., Donati J. F., 2019, MNRAS, 488, 5114
Klein B., Donati J. F., 2020, MNRAS, 493, L92
Kurucz R. L., 1993, SYNTHE Spectrum Synthesis Programs and Line Data CD-ROM No. 1. Smithsonian Astrophysical Observatory, Cambridge, MA
Landstreet J. D., Bagnulo S., Andretta V., Fossati L., Mason E., Silaj J., Wade G. A., 2007, A&A, 470, 685
Lavail A., Kochukhov O., Wade G. A., 2018, MNRAS, 479, 4836
Lehmann L. T., Hussain G. A. J., Vidotto A. A., Jardine M. M., Mackay D. H., 2021, MNRAS, 500, 1243
Lin D. N. C., Bodenheimer P., Richardson D. C., 1996, Nature, 380, 606
Lopez E. D., Fortney J. J., 2013, ApJ, 776, 2
Lopez E. D., Fortney J. J., 2014, ApJ, 792, 1
MacGregor M. A. et al., 2013, ApJ, 762, L21
Madhusudhan N., 2019, ARA&A, 57, 617
Mahmud N. I., Crockett C. J., Johns-Krull C. M., Prato L., Hartigan P. M., Jaffe D. T., Beichman C. A., 2011, ApJ, 736, 123
Malo L. et al., 2014, ApJ, 792, 37
Mamajek E. E., Bell C. P. M., 2014, MNRAS, 445, 2169
Mann A. W., Feiden G. A., Gaidos E., Boyajian T., von Braun K., 2015, ApJ, 804, 64
Mann A. W. et al., 2016, AJ, 152, 61
Martioli E. et al., 2020, A&A, 641, L11
Matthews B. C. et al., 2015, ApJ, 811, 100
Messina S. et al., 2016, A&A, 596, A29
Mordasini C., 2020, A&A, 638, A52
Mordasini C., Alibert Y., Georgy C., Dittkrist K. M., Klahr H., Henning T., 2012b, A&A, 547, A112
Mordasini C., Alibert Y., Klahr H., Henning T., 2012a, A&A, 547, A111
Morin J., Donati J. F., Petit P., Delfosse X., Forveille T., Jardine M. M., 2010, MNRAS, 407, 2269
Morin J. et al., 2008, MNRAS, 390, 567
Moutou C. et al., 2017, MNRAS, 472, 4563
Moutou C. et al., 2020, A&A, 642, A72
Nelson B. E. et al., 2020, AJ, 159, 73
Owen J. E., Wu Y., 2013, ApJ, 775, 105
Palle E. et al., 2020, A&A, 643, A25
Petit P., Donati J. F., Collier Cameron A., 2002, MNRAS, 334, 374
Petit P. et al., 2015, A&A, 584, A84
Plavchan P., Werner M. W., Chen C. H., Stapelfeldt K. R., Su K. Y. L., Stauffer J. R., Song I., 2009, ApJ, 698, 1068
Plavchan P. et al., 2020, Nature, 582, 497
Press W. H., Teukolsky S. A., Vetterling W. T., Flannery B. P., 1992, Numerical Recipes in FORTRAN. The Art of Scientific Computing. Cambridge Univ. Press, Cambridge
Queloz D. et al., 2001, A&A, 379, 279
Rajpaul V., Aigrain S., Osborne M. A., Reece S., Roberts S., 2015, MNRAS, 452, 2269
Rasmussen C. E., Williams C. K. I., 2006, Gaussian Processes for Machine Learning. MIT Press, Cambridge, USA
Reiners A., 2012, Living Rev. Solar Phys., 9, 1
Rodono M. et al., 1986, A&A, 165, 135
Saar S. H., 1994, in Rabin D. M., Jefferies J. T., Lindsey C., eds, IAU Symp. Vol. 154, Infrared Solar Physics. Kluwer Academic Publishers, Dordrech, p. 493
Sanz-Forcada J., Dupree A. K., 2008, A&A, 488, 715
Schmidt S. J., Kowalski A. F., Hawley S. L., Hilton E. J., Wisniewski J. P., Tofflemire B. M., 2012, ApJ, 745, 14
Scholz A., Coffey J., Brandeker A., Jayawardhana R., 2007, ApJ, 662, 1254
Schöfer P. et al., 2019, A&A, 623, A44
Semel M., 1989, A&A, 225, 456
Sezestre É., Augereau J. C., Boccaletti A., Thébault P., 2017, A&A, 607, A65
Shkolnik E., Liu M. C., Reid I. N., 2009, ApJ, 699, 649
Short C. I., Doyle J. G., 1998, A&A, 331, L5
Shulyak D., Reiners A., Engeln A., Malo L., Yadav R., Morin J., Kochukhov O., 2017, Nat. Astron. 1, 0184
Siess L., Dufour E., Forestini M., 2000, A&A, 358, 593
Strugarek A., Brun A. S., Matt S. P., Réville V., 2015, ApJ, 815, 111
Suárez Mascareño A. et al., 2020, A&A, 639, A77
Torres C. A. O., Ferraz Mello S., 1973, A&A, 27, 231
Tuomi M., Jones H. R. A., Barnes J. R., Anglada-Escudé G., Butler R. P., Kiraga M., Vogt S. S., 2018, AJ, 155, 192
Vidotto A. A., Bourrier V., 2017, MNRAS, 470, 4026
Vidotto A. A., Donati J. F., 2017, A&A, 602, A39
Vidotto A. A., Jardine M., Morin J., Donati J. F., Opher M., Gombosi T. I., 2014, MNRAS, 438, 1162
Weise P., Launhardt R., Setiawan J., Henning T., 2010, A&A, 517, A88
Wilner D. J., Andrews S. M., MacGregor M. A., Hughes A. M., 2012, ApJ, 749, L27
Wisniewski J. P. et al., 2019, ApJ, 883, L8
Yu L. et al., 2017, MNRAS, 467, 1342
Yu L. et al., 2019, MNRAS, 489, 5556
Zechmeister M., Kürster M., 2009, A&A, 496, 577
Zirin H., 1982, ApJ, 260, 655

APPENDIX A: FULL JOURNAL OF OBSERVATIONS

In addition to the journal of observation given in Table 1, we provide our measurements of RVs for the three methods presented in Section 3.1 and the time-series of activity indicators described in Section 6 in Table A1.

Downloaded from https://academic.oup.com/mnras/article/502/1/188/6027693 by CNRS - ISTO user on 02 February 2021

Table A1. Information on the spectropolarimetric observations of AU Mic with SPIRou. The first two columns indicate respectively the UT date and the BJD at mid-exposure of each observation. We then list the RVs measured by modeLling each Stokes *I* LSD profile by Gaussian function (reference RVs, column 3), computing the median bisector of each line (column 4), and fitting the first derivative of a Gaussian function to the median-subtracted line profiles (column 5; see Section 3.1 for further details about the RV measurement processes). The typical 1σ error bar on the RVs is $5\,\mathrm{m\,s^{-1}}$. The estimated RV photon noise σ_{ph} is listed in column 6. In columns 7 and 8, we give the values of the longitudinal field, B_ℓ, and the velocity span V_S, computed using the method described in Section 3.1 and featuring an error bar of $15\,\mathrm{m\,s^{-1}}$. Column 9 gives the FWHM of the Stokes *I* LSD profiles computed from the mask of atomic lines of Landé factors >1.5 (see Section 6). The last 3 columns respectively give the indicators based on He I, Paβ, and Brγ lines with $\pm1\sigma$ error bars (see Section 6). The flux variation of each line is given by $(1-\gamma)\times\delta l$, where γ is the activity index listed below, and δl us the spectral domain on which the index is computed, equal to 0.28, 0.18, and 0.4 nm, for He I, Paβ, and Brγ, respectively. The equivalent widths of the median He I, Paβ, and Brγ lines are respectively 0.006, 0.014, and ∼0.001 nm.

UT date	BJD [2457000+]	RV (Ref) [m s^{-1}]	RV (BIS) [m s^{-1}]	RV (LSD) [m s^{-1}]	σ_{ph} [m s^{-1}]	B_ℓ [G]	V_S [m s^{-1}]	FWHM [km s^{-1}]	He I	Paβ	Brγ
Sep/18	1744.8212	59.5	48.0	50.1	2.1	−43.9 ± 3.1	−63.1	0.38 ± 0.20	1.001 ± 0.005	1.000 ± 0.004	0.993 ± 0.010
Sep/24	1750.7542	−18.2	−12.0	−14.9	2.1	40.6 ± 3.7	0.0	0.00 ± 0.32	1.007 ± 0.005	1.018 ± 0.005	0.992 ± 0.013
Sep/25	1751.7453	−52.4	−66.1	−74.8	2.0	31.3 ± 3.2	65.1	−0.74 ± 0.12	1.037 ± 0.004	0.991 ± 0.004	1.003 ± 0.011
Sep/26	1752.7898	27.9	24.0	21.9	2.1	48.6 ± 2.9	−31.0	−1.36 ± 0.21	1.006 ± 0.005	0.991 ± 0.004	0.994 ± 0.010
Oct/2	1758.7288	51.3	41.0	46.5	2.2	16.2 ± 2.8	−30.0	−0.01 ± 0.14	0.969 ± 0.005	0.996 ± 0.004	0.993 ± 0.008
Oct/3	1759.8053	69.2	59.6	69.8	2.5	15.9 ± 3.2	−18.0	0.79 ± 0.13	1.028 ± 0.006	1.013 ± 0.004	0.995 ± 0.006
Oct/4	1760.7278	−29.6	6.0	15.2	2.8	48.5 ± 3.7	43.0	−0.14 ± 0.26	1.024 ± 0.007	1.004 ± 0.005	1.006 ± 0.008
Oct/5	1761.7305	−87.2	−90.1	−92.5	2.1	24.8 ± 2.9	19.0	−1.04 ± 0.17	1.037 ± 0.008	1.006 ± 0.005	0.997 ± 0.010
Oct/6	1762.7315	−2.9	0.0	2.8	2.1	52.6 ± 2.7	−45.0	0.11 ± 0.14	1.028 ± 0.006	1.004 ± 0.004	1.007 ± 0.010
Oct/8	1764.7571	34.5	48.0	62.7	2.1	23.6 ± 3.9	21.0	1.64 ± 0.25	1.017 ± 0.005	1.012 ± 0.004	1.014 ± 0.013
Oct/9	1765.7694	−39.8	−36.0	−35.1	2.0	34.4 ± 3.2	44.0	0.25 ± 0.22	1.020 ± 0.005	1.012 ± 0.004	1.014 ± 0.010
Oct/13	1769.7438	22.1	48.0	55.0	2.0	32.6 ± 3.1	5.0	0.88 ± 0.27	0.998 ± 0.006	1.006 ± 0.004	1.013 ± 0.009
Oct/14	1770.7407	−41.6	−42.0	−33.6	2.2	33.4 ± 3.4	16.0	−0.32 ± 0.17	1.012 ± 0.004	1.000 ± 0.003	1.000 ± 0.008
Oct/15	1771.7212	−55.8	−30.0	−36.2	2.3	16.4 ± 3.1	61.1	−0.89 ± 0.19	1.016 ± 0.005	1.000 ± 0.003	1.013 ± 0.007
Oct/16	1772.7416	19.4	24.0	31.1	2.4	47.2 ± 3.4	−103.1	0.48 ± 0.31	0.984 ± 0.005	0.995 ± 0.003	0.983 ± 0.009
Oct/31	1787.7155	28.3	6.0	4.1	2.5	−4.7 ± 3.2	−57.1	1.55 ± 0.19	0.971 ± 0.005	0.979 ± 0.004	0.999 ± 0.007
Oct/32	1788.7045	41.3	60.1	58.5	2.3	4.2 ± 3.3	−96.1	1.16 ± 0.20	0.986 ± 0.005	0.992 ± 0.004	0.990 ± 0.006
Nov/2	1789.7367	−32.6	−24.0	−22.3	2.1	82.5 ± 3.2	43.0	−0.80 ± 0.19	0.991 ± 0.004	0.997 ± 0.004	1.000 ± 0.007
Nov/3	1790.7010	−90.1	−90.1	−85.0	2.1	12.4 ± 3.6	75.1	−1.46 ± 0.15	1.009 ± 0.005	1.006 ± 0.004	1.012 ± 0.012
Nov/4	1791.6983	2.1	0.0	5.6	2.1	40.3 ± 2.8	31.0	−0.67 ± 0.14	0.989 ± 0.005	0.992 ± 0.004	0.994 ± 0.007
Nov/5	1792.6976	19.1	18.0	18.8	2.0	−24.3 ± 3.1	−30.0	0.42 ± 0.16	0.976 ± 0.003	0.975 ± 0.004	0.988 ± 0.007
Nov/9	1796.6859	−13.5	−24.0	−24.3	2.7	43.7 ± 3.6	−56.6	0.18 ± 0.15	0.974 ± 0.007	1.001 ± 0.004	1.000 ± 0.008
Nov/10	1797.7098	19.7	37.5	56.6	2.7	−48.0 ± 3.7	27.0	−0.07 ± 0.35	0.969 ± 0.007	0.987 ± 0.007	0.989 ± 0.011
Nov/11	1798.6873	27.0	36.0	38.2	2.5	69.5 ± 3.5	−47.0	1.71 ± 0.10	0.978 ± 0.004	0.995 ± 0.004	1.007 ± 0.005
Nov/12	1799.6883	−10.3	−30.0	−30.3	2.7	70.0 ± 3.9	−28.0	0.60 ± 0.24	0.998 ± 0.006	1.010 ± 0.006	0.999 ± 0.009
Nov/13	1800.6896	−46.2	−42.0	−56.5	2.1	8.8 ± 3.0	34.0	−0.66 ± 0.24	1.001 ± 0.006	1.012 ± 0.005	1.001 ± 0.009
Nov/14	1801.6873	0.0	−12.0	−12.2	2.2	44.3 ± 3.2	−33.0	−0.13 ± 0.18	0.997 ± 0.006	1.002 ± 0.006	1.009 ± 0.011

APPENDIX B: SIMULATING THE MODELLING OF OUR RV TIME-SERIES INCLUDING EXCESS UNCORRELATED NOISE

We built a synthetic RV curve containing the GP prediction of the stellar activity signal (in the case of the reference RVs, i.e. line 1 of Table 4) and a planet signature of semi-amplitude $8.5\,\mathrm{m\,s^{-1}}$. From this curve, we created two different data sets, called S1 and S2, containing respectively $N = 100$ evenly sampled data points and $N = 27$ data points at the same epochs as our observations. In both cases, we added a random noise including a photon noise of $2\,\mathrm{m\,s^{-1}}$ rms, an additional uncorrelated Gaussian noise of $4\,\mathrm{m\,s^{-1}}$ rms, and finally set the 1σ RV uncertainties on each synthetic data point to $5\,\mathrm{m\,s^{-1}}$. We then ran our estimation process, including a fit of the excess uncorrelated noise *S* (see Section 3.3), on 40 of these simulated data sets, each with a different noise realization. Ideally, one would expect *S* to be null, given that the assumed formal error bars already account for the injected noise.

The resulting distribution of *S* is shown in Fig. B1. Whereas no significant excess noise is recovered in case S1 (mean value of 0.7 ± $0.2\,\mathrm{m\,s^{-1}}$), *S* is systematically overestimated in case S2, with a mean recovered value of 4.5 ± $2.0\,\mathrm{m\,s^{-1}}$. This suggests that the value of *S* we derived from our data, found to be $6.0^{+3.8}_{-3.1}\,\mathrm{m\,s^{-1}}$, that is, consistent with the average value of $4.5 \pm 2.0\,\mathrm{m\,s^{-1}}$ recovered in our simulations, is most likely overestimated.

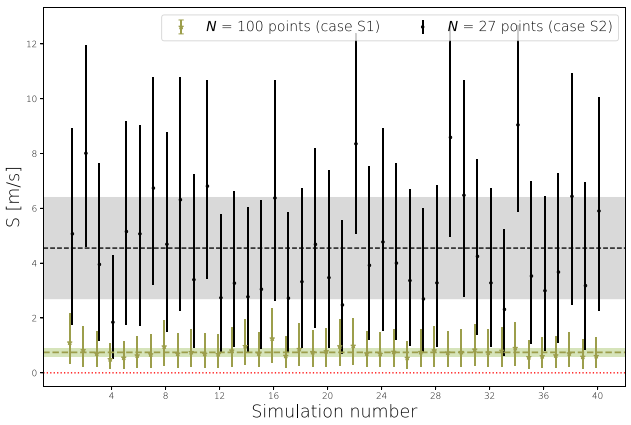

Figure B1. Best estimates of *S* obtained when modelling 40 simulated RV times-series, containing either 27 points (case S2, black dots) or 100 points (case S1, green stars), using the estimation process described in Section 3.2. The value of *S* to recover (i.e. $0.0\,\mathrm{m\,s^{-1}}$) is indicated by the red dotted line, whereas the mean values (respectively, standard deviations) of *S* recovered in cases S1 and S2 are respectively indicated by green and black dashed lines (respectively, light green and grey bands). For clarity, the *S* values obtained in case S1 are slightly shifted horizontally from those obtained in case S2.

Downloaded from https://academic.oup.com/mnras/article/502/1/188/6027693 by CNRS - ISTO user on 02 February 2021

Table C1. Results of the fit to the time-series of the activity indicators analysed in Section 6. The first two lines are respectively the typical formal uncertainty in the time-series ($\bar{\sigma}$), and the excess of uncorrelated noise recovered by the model. Lines 3–7 list the best estimates of the four hyperparameters (written in bold when fixed in the MCMC process), and the constant offset. Finally, we give the χ^2_r of the MCMC fit in line 7.

Indicator	RVs	B_ℓ	V_S	FWHM	He I	Paβ
$\bar{\sigma}$	$5\,m\,s^{-1}$	3.2 G	$15\,m\,s^{-1}$	$0.19\,km\,s^{-1}$	0.005	0.004
S	$6.0^{+3.8}_{-3.1}\,m\,s^{-1}$	$4.4^{+2.7}_{-2.4}$ G	$16^{+13}_{-10}\,m\,s^{-1}$	$0.55^{+0.21}_{-0.19}\,km\,s^{-1}$	$0.010^{+0.003}_{-0.002}$	0.006 ± 0.002
θ_1	$43^{+11}_{-8}\,m\,s^{-1}$	68^{+40}_{-27} G	$36^{+11}_{-8}\,m\,s^{-1}$	$0.9^{+0.4}_{-0.3}\,km\,s^{-1}$	0.03 ± 0.01	$0.011^{+0.006}_{-0.004}$
θ_2 (d)	**100**	105^{+67}_{-60}	**100**	**100**	**100**	**100**
θ_3 (d)	4.84 ± 0.01	4.83 ± 0.02	$4.89^{+0.04}_{-0.02}$	4.84 ± 0.04	$4.87^{+0.06}_{-0.05}$	$4.99^{+0.11}_{-0.09}$
θ_4	**0.4**	$0.7^{+0.4}_{-0.2}$	$0.36^{+0.17}_{-0.12}$	**1.0**	**1.0**	**1.0**
Constant offset	$0^{+19}_{-18}\,m\,s^{-1}$	44^{+61}_{-39} G	$4 \pm 26\,m\,s^{-1}$	$0.0 \pm 0.6\,km\,s^{-1}$	1.00 ± 0.02	1.00 ± 0.01
χ^2_r	0.8	0.8	4.0	7.8	3.2	2.4

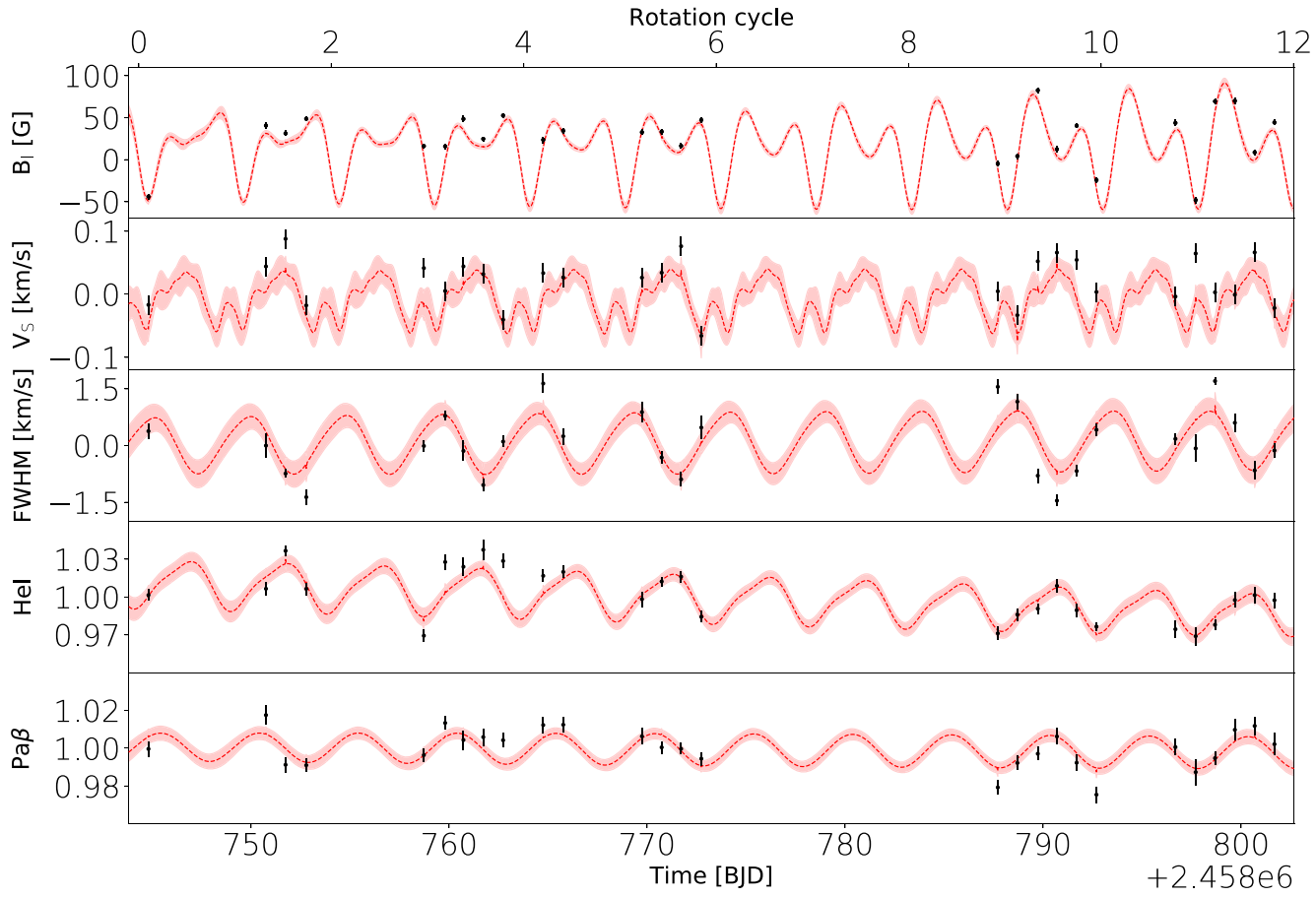

Figure C1. Best GP predictions (red dotted lines with $\pm 1\sigma$ error bands) of the time-series of each indicator analysed in Section 6 (black dots). The estimation of the hyperparameters of the GP (i.e. $\boldsymbol{\theta}$) is carried out following the method described in Section 3.2 and adopting the prior densities detailed in Section 6.

APPENDIX C: MODELLING ACTIVITY INDICATORS

To complement the analysis of stellar activity indicators of Section 6, we give results of the GP fit to the time-series of B_ℓ, V_S, FWHM, He I, Paβ in Table C1, and show the best prediction in Fig. C1. Brγ, that does not appear rotationally modulated, is not displayed here. We also plot each pair of activity indicator and give the associated Pearson correlation coefficient in Fig. C2.

Downloaded from https://academic.oup.com/mnras/article/502/1/188/6027693 by CNRS - ISTO user on 02 February 2021

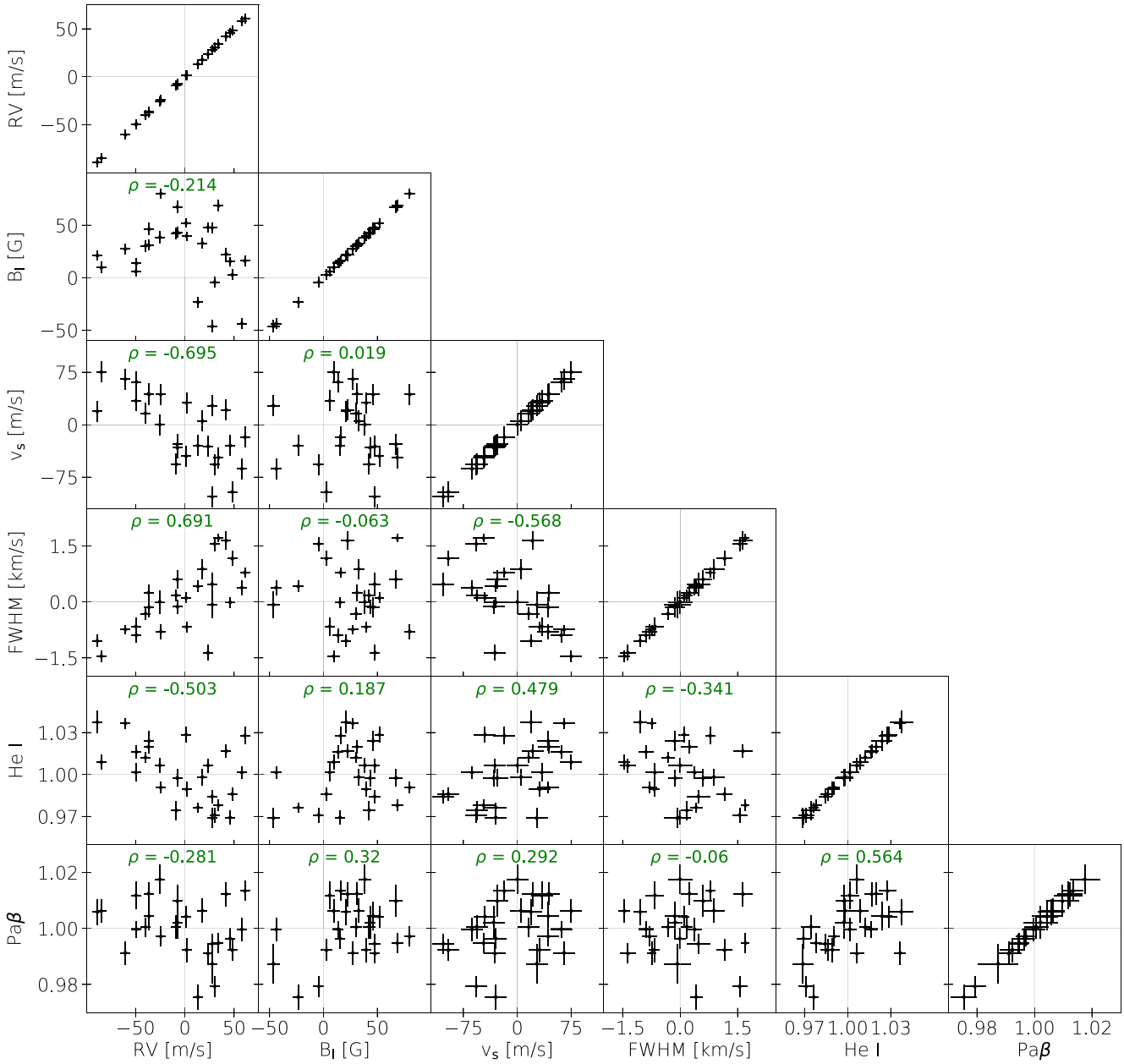

Figure C2. Correlation plots of the of activity indicators analysed in Section 6. The Pearson correlation coefficient, ρ, is written in green at the top of each panel.

This paper has been typeset from a TEX/LATEX file prepared by the author.

Downloaded from https://academic.oup.com/mnras/article/502/1/188/6027693 by CNRS - ISTO user on 02 February 2021